12-2010

Destructive Testing and Finite-Element Modeling of Full-Scale Bridge Sections Containing Precast Deck Panels

Travis R. Brackus

DESTRUCTIVE TESTING AND FINITE-ELEMENT MODELING OF FULL-SCALE BRIDGE SECTIONS CONTAINING PRECAST DECK PANELS

by

Travis R. Brackus

A thesis submitted in partial fulfillment
of the requirements for the degree

of

MASTER OF SCIENCE

in

Civil and Environmental Engineering

Approved:

_____	_____
Dr. Paul Barr Major Professor	Dr. Marvin Halling Committee Member
_____	_____
Dr. Joseph Caliendo Committee Member	Dr. Byron Burnham Dean of Graduate Studies

UTAH STATE UNIVERSITY
Logan, Utah

2010

ABSTRACT

Destructive Testing and Finite-Element Modeling of Full-Scale Bridge Sections Containing Precast Deck Panels

by

Travis R. Brackus, Master of Science

Utah State University, 2010

Major Professor: Dr. Paul Barr
Department of Civil and Environmental Engineering

Full-depth, precast panel deck systems are becoming more common in bridge installation and repair. The objective of these systems is to achieve the performance of cast-in-place systems while simultaneously saving time and money. The structural behavior of these systems has been the subject of scrutiny in recent research. The Utah Department of Transportation demolished a steel I-girder bridge containing a precast panel deck system and provided two full-scale specimens for this project. Destructive testing was performed at Utah State University on the specimens to investigate three failure modes: flexural, beam shear, and punching shear. Finite-element models were created using *ANSYS* software to replicate experimental behavior. Overall, it was found that the elastic, post-elastic, and ultimate behavior of the full-scale bridge sections containing precast panel deck systems can be accurately predicted in analytical models.

Another aspect of this project was to investigate changes in dynamic behavior as the system was subjected to flexural yield and failure. Point loads were applied and removed in increments, and dynamic testing was conducted at each load level. It was found that significant damage is somewhat noticeable by monitoring the changes in natural frequencies.

(124 pages)

ACKNOWLEDGMENTS

First, I would like to thank my parents, Gene and Michele Brackus, for their unconditional support throughout my life. Thanks to the Utah Department of Transportation for providing the bridge specimens. Thanks to the Utah Transportation Center for funding this project.

I owe special thanks to the members of my graduate committee: Dr. Paul Barr, Dr. Marvin Halling, and Dr. Joseph Caliendo. During my education at Utah State University they have inspired me to find a passion for civil engineering, and they have been incredibly resourceful for this project.

Thanks to Zane Wells for his arduous assistance in the testing process. Thanks to Ken Jewkes for helping with instrument calibration and material specimen testing, and for the use of machinery in his laboratory.

Lastly, I would like to thank Wesley Cook for many reasons. I thank him for the collaboration, enthusiasm, and overall effort he brought to this project. It would not have been possible without him.

Travis R. Brackus

CONTENTS

LIST OF TABLES

LIST OF FIGURES

LIST OF SYMBOLS

a	depth of Whitney stress block [mm (in.)]
b	width of Whitney stress block [mm (in.)]
E_c	elastic modulus of concrete [MPa (ksi)]
E_s	elastic modulus of steel [MPa (ksi)]
ft	feet
f'c	compressive strength of concrete [kPa (psi)]
f_c	compressive stress of concrete [kPa (psi)]
f_r	tensile strength of concrete [kPa (psi)]
f_u	ultimate stress of steel [MPa (ksi)]
f_y	yield stress of steel [MPa (ksi)]
Hz	Hertz [cycles per second]
in.	inches
k	kip
k-ft	kip-feet
kN	kiloNewtons
kN-m	kiloNewton-meters
kPa	kiloPascals
ksi	kips per square inch
L	overall girder length
m	meters
mm	millimeters

MPa	megaPascals
psi	pounds per square inch
β_c	shear transfer coefficient for closed cracks
β_t	shear transfer coefficient for open cracks
$\mu\varepsilon$	microstrain [mm^{-6}/mm (in^{-6}/in)]
ν	Poisson's ratio
θ	angle measured from x-axis towards y-axis [°]
φ	angle measured from x-y plane to z-axis [°]
°	degrees
’	minute [°/60]
”	second [°/3600]

CHAPTER I

INTRODUCTION

The Utah Department of Transportation (UDOT) has recently implemented an accelerated bridge construction (ABC) program for the installation and repair of bridges throughout the state. The ABC program utilizes many advanced design and construction techniques. An integral component of this program involves the use of full-depth precast deck panels for bridge systems. Much of the construction involving the reinforced concrete can be performed off-site, thereby reducing the need for extended traffic closures. The deck panels can then be lifted into place in hours as opposed to days or even weeks that it takes for conventional construction. Transportation departments throughout the nation are taking advantage of precast panel deck systems in one form or another. The increased use of precast deck panels coupled with the limited performance data amplifies the importance of understanding their structural behavior.

The 8th North Bridge located in I-15 in Salt Lake City was constructed in the 1960's by UDOT. In 2007, due to excessive deterioration, the concrete deck of the 8th North Bridge was removed and replaced with an ABC precast panel deck system. In the fall of 2009, the bridge was replaced due to a separate expansion project. Because of the unique history of the bridge the Utah Transportation Center (UTC) funded this project and two sections of the 8th North Bridge were salvaged for this research. These two, full-scale bridge sections provided a rare opportunity to study the behavior of a steel I-girder bridge system built with ABC precast deck panels after two years of service.

Full scale destructive testing of in-service bridge components is rare. However, as design and construction technologies advance, the behavioral understanding of these new tools must progress accordingly. Engineers must be able to predict service behavior as well as ultimate capacities of various failure modes to ensure the safety and design efficiency of modern bridges. While nearly all engineers have access to finite-element modeling programs that can accomplish such a task, there exist no code provisions regarding the construction of the models (i.e. element types, boundary conditions, etc.). The first purpose of this project was to determine the structural behavior, both static and dynamic, of a steel I-girder composite bridge by full-scale destructive testing, of which multiple failure modes were to be tested. The second purpose of this project was to develop analytical modeling criteria that could reproduce experimental results. The structural aspects investigated in this research are:

1. The elastic and post-elastic flexural behavior of the system.
2. The beam-shear capacity of the system.
3. The punching-shear capacity of the precast deck panels.
4. The changes in dynamic response through flexural failure.

CHAPTER II

LITERATURE REVIEW

Bridges are becoming more complex as our transportation infrastructure gets progressively restored. Not only must we understand the performance of these bridges within design limits, but post-elastic behavior is important as well. Ultimate capacities of bridges not only arise in the design stage (strength design), but also in the cases of a retrofit or damage assessment project. To ensure safety of roadway users, it is crucial that engineers have a firm grasp on bridge behavior throughout its loading range.

The finite-element method has aided researchers in predicting the structural behavior of different types of bridges. A properly constructed finite-element model (FEM) can predict service behavior and ultimate strength capacities of a structure with sufficient accuracy. Chapter 2 briefly illustrates this concept by presenting studies in which the researchers used finite-element analysis (FEA) to complete their investigations. The summaries of the following publications demonstrate both the applicability of FEA in terms of bridge research as well as the procedural aspects of employing such an advanced tool.

Mabsout et al. (1997)

The researchers investigated the accuracy of various modeling schemes to determine sufficient modeling criterion for slab on girder bridge systems. Four finite-element modeling schemes were compared with each other. The research was focused on

the distribution of service loads. Two software programs were used to analyze the four modeling techniques.

The four finite-element modeling schemes had consistent nodal geometries, support conditions, and loading patterns; however, the types of elements used in the models varied. The first three models were created in the software, *SAP90*, and the fourth was created in the software, *ICES-STRUDL*. In Case A, the concrete slab was modeled using four-node shell elements and the steel girders were modeled using two-node frame members. The centroid of the girders coincided with the centroid of the concrete slab; however, the flexural properties of the girders were transformed to account for the slab-girder eccentricity. Case B was similar to Case A in that the concrete slab was modeled the same (shell elements), but Case B accommodated the eccentricity of the steel girders. Rigid links were used to connect the frame elements (girders) to the shell elements (deck), to represent composite action between the two. In Case C, shell elements were used for the concrete deck and the webs of the steel girders, while the girder flanges were modeled using frame elements. Rigid links were used to model the flange-to-deck eccentricity, similar to Case B. In Case D the concrete slab was modeled with an eight-node solid brick element and the girders were modeled with four-node shell elements.

Case A (frame and shell modeling) involved the least number of nodes relative to the other three cases and hence required less computational time. This modeling scheme was implemented and substantiated with previous publications of slab on girder bridge

tests. It was determined that the elastic behavior of bridge systems could be accurately modeled using shell elements for the deck and frame elements for the girders.

Barbosa and Ribeiro (1998)

The finite-element modeling of concrete in its nonlinear range has proven to be difficult. A new concrete material model was adopted by *ANSYS* that predicted brittle failures. The researchers investigated this concrete material model in a computer study. The goal was to find the most accurate and practical modeling criterion to represent reinforced concrete structures.

A simply supported reinforced concrete beam was the case study. A uniformly distributed line load was applied to the beam. The strategy was to use various material models and recorded the load-deflection data for each model. The analytical deflections were calculated using a nonlinear moment-curvature analysis. The computer predicted deflections were then compared against analytical deflections. An experimental model was not completed at the time of this study.

Two reinforcing options were used for steel: discrete reinforcement and smeared reinforcement. In discreet reinforcement, the individual steel elements were input as separate elements from concrete. In smeared reinforcement, a volumetric ratio of steel was defined for the solid elements. The resulting element stiffness was a combination of steel and concrete.

The material models for concrete all included a linear elastic region. From there, various nonlinear assumptions were implemented. The post-elastic assumptions

included: perfectly plastic, multi-linear work hardening, and crushing. The perfectly plastic model is defined by the Drucker-Prager failure criterion, which assumes a conical failure surface that is exhibited in granular materials such as soil and concrete. The crushing feature is encompassed in the concrete material model in *ANSYS*. It is defined by a bi-axial compressive stress failure envelope. When the maximum principal stresses at a Gauss integration point exceed this envelope, the element stiffness is set to zero at that integration point. The load is then transferred to surrounding elements. The brittle concrete model also has a cracking feature which uses the same principles as the crushing feature except that failure is defined by a maximum tensile stress. When the minimum principal stress at an integration point exceeds the tensile stress, the element is cracked at that integration point.

All models constructed showed good correlation in the elastic range. For the models that included the cracking feature, there was an initial jump in the early stages of loading corresponding to initial cracking. Other than that, all models exhibit nearly the same stiffness up through service load. At that point, the results vary.

Models assuming linear elasticity and crushing fail to converge soon after service loading. These models fail to predict any post-elastic deflections because of the unconverged solution. The elastic-perfectly plastic model defined by the Drucker-Prager yield criterion behaved in a similar manner. Ultimately, these two models predicted an ultimate capacity well below that of the analytical plastic capacity.

Models that include work hardening for concrete produce longer load-deflection histories. The only model to predict an ultimate load remotely close to the theoretical

capacity consisted of a linear elastic/perfectly plastic/work hardening stress-strain curve for concrete. Regardless whether the reinforcement was modeled discretely or smeared within the concrete elements, this material model generated load-deflection plots that correlate very closely to the theoretical analysis.

The final observation in the study involved a convergence issue. It was found that models combining crushing and plasticity are unable to converge to a solution at a relatively low load level. The researchers suggest that there is some degree of incompatibility in the *ANSYS* concrete model between yielding and failure.

Fu and Lu (2003)

The primary design technique employed by bridge engineers is the traditional transformed section method. This tool assumes complete linear elasticity which is satisfactory for the behavior of steel girders under service loads. However, concrete remains a nonlinear material with very low tensile strength. Fu and Lu present an accurate numerical nonlinear modeling procedure to predict post-elastic bridge behavior. A *FORTRAN* computer program was written to carry out the modeling.

There were three critical components of the model: the steel girders, the shear studs, and the concrete deck. The steel girders were modeled by planar elements. Plate elements were used for the flanges and membrane elements were used for the web Different element types were used for the girder flanges and web to reduce the number of degrees of freedom (DOF's) in the overall stiffness matrix. The girders were intended to remain in the elastic working range of steel and hence no nonlinearities were introduced.

The shear studs were implemented to the numerical model as bar elements connecting the top flanges to the deck. The bar elements were idealized as two independent linear springs. The springs had a normal stiffness defined by a linear constitutive relationship and a tangential stiffness which was a function of the slip on the girder/deck interface. The function was decayed exponentially (i.e. more slip resulted in lower stiffness).

The concrete deck was modeled using two dimensional plate elements. Reinforcement was provided by similar plate elements of equivalent smeared steel. To satisfy the purpose of the research the modeling of concrete deck focused on its compressive nonlinearity, lack of tensile strength, and biaxial loading behavior. The former two was represented by a stress-strain curve while the latter required a principal stress failure envelope.

Computation of nonlinear behavior inherently suggests an incremental algorithm in which the constitutive relationships are modified during the stiffness matrix calculations. The researchers used the modified Newton-Raphson method and divided the load into increments. For one increment, the stiffness matrix was calculated and the global equilibrium equation was solved. In the Newton-Raphson method, a solution is first approximated and the function is solved. In the research, the approximation resulted in force imbalances in the global stiffness equation. These imbalances were redistributed as nodal loads and the solution process was repeated. When the force imbalance was within a tolerable range (close to zero) the solution was said to have converged, at which point the next loading increment was considered. The element stiffness matrices were

calculated at each iteration using a Gauss numerical integration rule. The stresses at the Gauss points were continuously checked with the biaxial failure envelope for cracking or crushing. Upon failure limit the elasticity modulus of the element was set to zero which introduced more force imbalances.

The modeling scheme was validated by experimental deflection data of a test bridge. These results are compared to those calculated by the transformed section method as prescribed by the American Association of State and Highway Transportation Officials (AASHTO). It was shown that the experimental and FEM deflections were consistent and the transformed section method deflections were very conservative. The nonlinear modeling procedure implemented in the research was thus verified.

Issa et al. (2007)

The researchers performed full-scale testing of a prefabricated, full-depth, precast concrete deck panel bridge to investigate the structural behavior and constructability of such systems. Among other evaluations, this research was geared towards serviceability and functionality of the precast concrete panels, transverse joint behavior, shear connector behavior, and the effects of longitudinal post-tensioning on transverse joints. A full-scale bridge was designed, constructed, and tested to accomplish the aforementioned objectives.

The design of all components of the bridge was in accordance with AASHTO standards. The bridge was a two-span, two-lane, continuous system that consisted of precast reinforced concrete panels installed upon three steel beams. The individual

precast panels were connected by post tensioning in the transverse joints. Nelson shear studs were grouted into shear pockets to obtain composite action. The bridge was simply supported on the ends with a fixed support at the intermediate location.

The structural response of the bridge during testing was monitored and recorded continuously using a data acquisition system. Linear variable displacement transducers were used on the middle beam to measure the deflections of the maximum positive and negative moment locations. Strain gages were mounted at the same locations and at the middle support. The strain gages were placed at the top and bottom of the slab, throughout the depth of the middle steel beam, and some were embedded in the concrete panels prior to the casting process. Hydraulic rams and rigid loading frames were used to apply loads to the bridge. The location of the loading was predetermined to generate the maximum design positive and negative moments in the bridge. Three load tests were performed: service, overload, and ultimate. In all load scenarios, strain gage data indicated that the system maintained full composite action throughout loading up to about 94% of the ultimate load.

Experimental results were supported with the modeling of the bridge system using nonlinear FEA. The software, *ANSYS*, *Version 9*, was used to create the FEM. The authors took advantage of the bridge's symmetry when creating the model to reduce computational time by only considering half of the bridge with the appropriate boundary conditions (i.e. pinned-fixed). Finite-element analysis overestimated the ultimate capacity of the bridge by 12.6%. At the experimental ultimate load, the finite element deflections were within 1.2% of the experimental deflections. Furthermore, strain values

generated by the model confirmed the experimental finding that full composite action was maintained between the concrete and steel system through failure.

Chen, Spyrakos, and Venkatesh (1995)

Nondestructive damage evaluation (NDE) is becoming more widely used to assess the structural integrity of bridges. This is typically carried out by analyzing the dynamic response of the bridge system by modal analysis, and more importantly, how the dynamic response changes as the bridge deteriorates. The stiffness of the structure tends to decrease with an increase in damage, resulting in lower natural frequencies. The researchers examined this effect by monitoring the dynamic behavior of steel beams which were progressively damaged.

The objective of the project was geared towards bridge research; therefore, the researchers experimented on simply supported, steel channel beams which had dynamic properties similar to that of a full size bridge. The undamaged beams were subjected to point loads at certain predetermined locations to excite several low vibration modes. The load was quickly removed, and the beams were allowed to freely. An accelerometer was mounted to the beams, and a signal analyzer connected to an industrial computer collected and processed the data. The data was converted from the time domain to the frequency domain using a fast Fourier transform (FFT). Natural frequencies and corresponding mode shapes were then determined.

Damage was inflicted to the beams by cutting notches out of the flanges; thereby reducing its load-carrying capacity. The level of damages was indexed as a ratio of the

design strength to the plastic strength of the section. Consequently, a damage index of unity would indicate formation of a plastic hinge should the structure be subjected to its design load. A dynamic test was performed at each damage level, and the natural frequencies and corresponding mode shapes were recorded. At a damage index of unity, the first four modal frequencies decreased by 4.9%, 2.0%, 2.9%, and 3.0% from the undamaged state, respectively.

Finite element models were created in the software, *SAP IV*, for the undamaged and damaged beams. Three-dimensional beam elements with six degrees of freedom (DOF's) at each node were used for all elements in all cases. The software analyzed each model and calculated its global natural frequencies and mode shapes. From the undamaged state to a damage index of unity, the FEA predicted decreases in modal frequencies consistent with, but smaller than the aforementioned experimental values.

The research clearly illustrated that shifts in natural frequencies could be used to detect damage in structural systems; however, it has been shown that natural frequencies of an active bridge can vary as much as 10% over the course of a year (Askegaard and Mossing, 1988). Because of this, the researchers concluded that changes in natural frequency are an unreliable indicator of the structural integrity of bridges.

Lauzon and DeWolf (2006)

The Connecticut Department of Transportation funded this project to explore bridge monitoring systems in order to predict catastrophic failures. The researchers used nondestructive damage evaluation (NDE), which conventionally relies on modal analysis

of the structure and must be conducted where no traffic is on the bridge. In Connecticut, heavy traffic volumes prevent such tests from being justifiable; therefore, the researchers investigated the dynamic response of a full scale bridge subjected to excitation provided by ambient vehicle vibrations. A bridge was salvaged and made available for this project.

The experimental bridge specimen was an excision of a larger system. It consisted of a concrete deck supported by three girders with a single parapet along one side. Accelerometers were mounted on the underside of the bridge girders. A full-size truck was driven across the bridge, and the vibrations were recorded by the accelerometers. Data was acquired by a Digital Instrumentation Tape Recorder in the time domain. The data was analyzed and converted to the frequency domain. The test was conducted 15 times to establish proper natural frequencies and mode shapes. Damage was then inflicted to the system by cutting into the exterior girder, representing a large crack. The crack was introduced in five steps: first cutting the entire bottom flange, and then incrementally cutting into the web. The ambient vibration test was repeated at each stage, and new natural frequencies were calculated.

The researchers found that both the natural frequency value and amplitude of the FRS at the peaks were sensitive to the damage inflicted. For the first damage stage (entire flange cut), the amplitude of the FRS plot for the first mode shape increased 77%. Other modes and damage stages showed similar behavior, although to lesser extents. Results indicate that there is a less noticeable shift in natural frequencies with increased damage states. A maximum of 7.6% change in natural frequency from the undamaged

state was recorded. The researchers wished to investigate the change in mode shapes of the structure, if any; however, their data acquisition system was limited to eight channels, and sufficient mode shapes could not be determined. Overall, the research showed a promising outlook for the use of NDE to detect damage in bridges.

CHAPTER III

LABORATORY EXPERIMENTS

This chapter presents, in detail, the laboratory experiments conducted on the I-15/8th North Bridge sections. Two bridge specimens were tested through various modes of failure. The failure modes consisted of single-girder flexural, single-girder shear, and punching shear of the concrete deck. Dynamic testing was also conducted one of the specimens to determine the natural frequencies and corresponding mode shapes of the bridge system through yield and failure. Finite-element models were created to reproduce experimental results (discussed in Chapter 4).

Chapter 3 is divided into five sections. The first section describes the I-15/8th North Bridge history and the geometry of the salvaged specimens. The next three sections present the flexural, beam shear, and punching shear tests, respectively. The final section presents the dynamic testing.

Bridge Specimen Description

The I-15/8th North Bridge was a two lane overpass in Salt Lake City owned and managed by UDOT. The original bridge was constructed in the 1960's with six steel girders with a reinforced cast-in-place deck system. The four-span bridge spanned in the east-west direction over Interstate 15. The bridge roadway was slightly curved; however, the girders were straight in each span and kinked at supports (Figure 1).

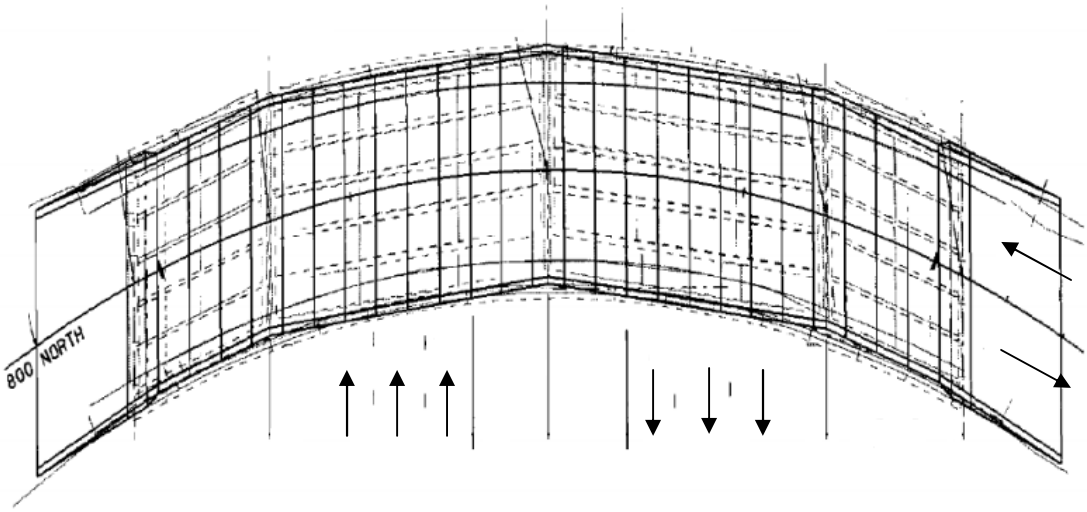

Figure 1. I-15/8th North Bridge layout (UDOT, 2006).

Figure 2. Looking northeast at deck replacement.

After forty-plus years of service, the concrete deck had deteriorated to the point where a deck replacement was necessary. In 2007, the concrete was stripped away while the original steel girders were left in place as they were in good condition. Custom reinforced concrete deck panels were cast near the site. The panels were installed transversely on the bridge as shown in Figure 2. This was the first project in which UDOT had implemented precast deck panels.

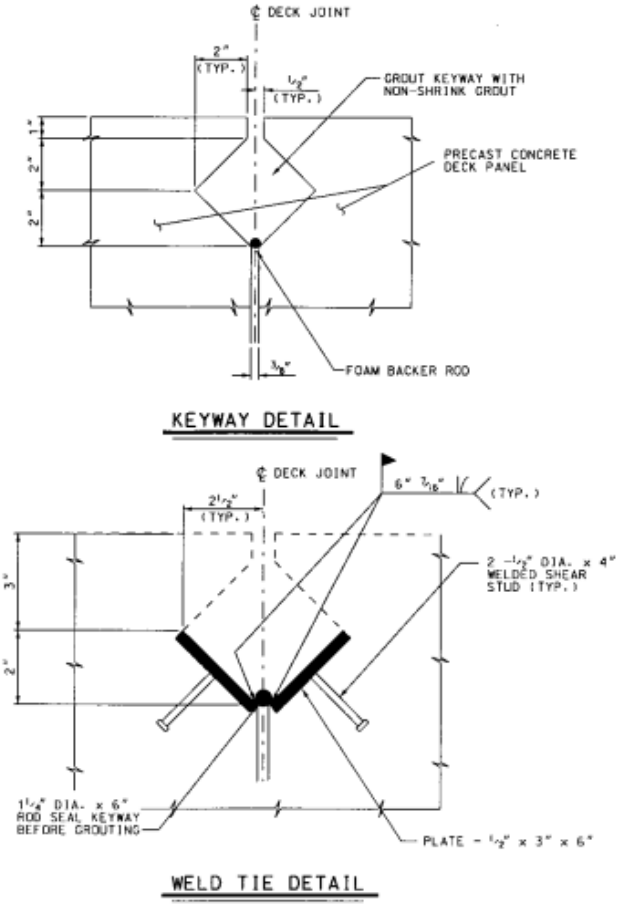

Figure 3. Transverse female-to-female joint connection (UDOT, 2006).

Specifications of the bridge were provided by UDOT from as-built drawings of the deck replacement project. The deck consisted of 197 mm (7.75 in.) thick, full-depth precast panels. The panels were as long as the bridge was wide, or 13.31 m (43 ft 8 in.), and had a width of 2.41 m (7 ft 10.75 in.). The panels were attached together by transverse female-to-female joint connections which occurred approximately every 610 mm (24 in.) along the panel-to-panel interface (Figure 3). There was approximately a 76.2 mm (3.0 in.) cover of asphalt above the concrete deck. The deck system was connected to steel girders by nelson shear studs that were grouted into shear pockets of the concrete panels. The shear pockets occurred every 457mm (18 in.) on center above each girder.

In 2009, the bridge was demolished in accordance with the Beck Street expansion project. At that time, UDOT supplied funding and requested that two specimens of the bridge be salvaged and made available for this research project. This provided a rare opportunity to conduct full-scale destructive testing on a bridge containing precast deck panels after two years of service.

Two sections of Span 1of the 8th North Bridge were excised from the field for this research project. The concrete deck was cut on opposing sides of adjacent girders. The concrete cuts were made parallel to traffic flow and girder centerlines (Figure 4). The bridge deck of Specimen 1 measured approximately 11.68 m (38 ft 4 in.) longitudinally by 3.24 m. (10 ft 7.75 in.) transversely and the bridge deck of Specimen 2 measured 11.67 m (38 ft 3 in.) longitudinally by 3.21 m (10 ft 6.5 in.) transversely.

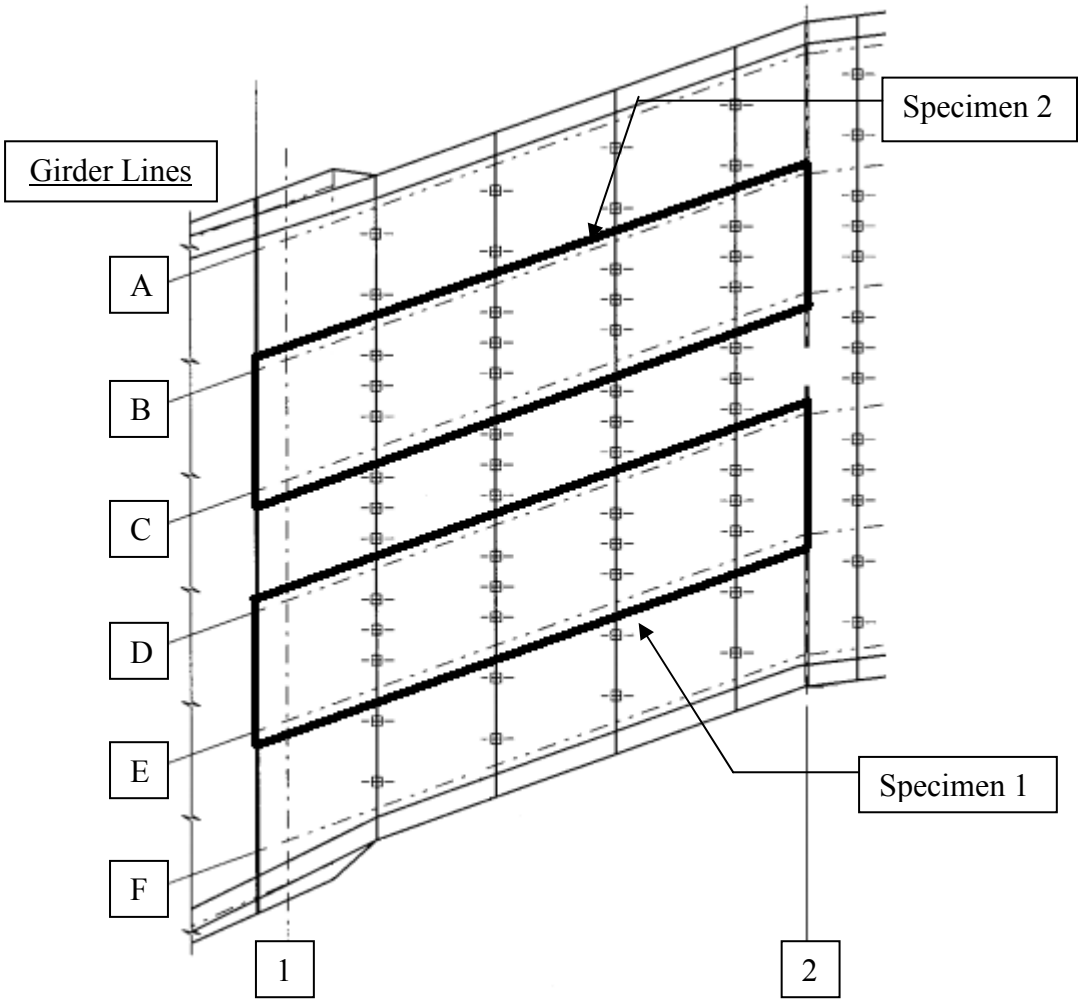

Figure 4. Plan view of salvaged bridge sections (west span).

Note the girder centerline callouts in Figure 4, which will serve as the girder naming convention throughout this paper. Specimen 1 contained Girders D and E while Specimen 2 contained Girders B and C. Also note the vertical lines 1 and 2, which will designate the ends of the girders throughout this paper. All girders tested had identical geometries. The girders were 10.9 m (35 ft 9 in.) long. The girders were built-up sections with flange plates measuring 254 mm (10.0 in.) by 15.9 mm (0.625 in.) in cross

section and web plates measuring 965 mm (38 in.) by 9.5 mm (0.375 in.) in cross section. The webs of the girders were singly stiffened with 9.5 mm (0.375 in.) thick plates located at 0.91 m (3.0 ft) on center. On the un-stiffened side of the girders, there were three stiffeners: on either end and at mid-span. The as-built drawings called out a transverse super-elevation of 4% and a skew angle of 19° 36' 59", which was consistent with that of the deck cutouts. Each specimen contained three equally spaced transverse diaphragms which were C380X15.4 (C15X33.9) sections.

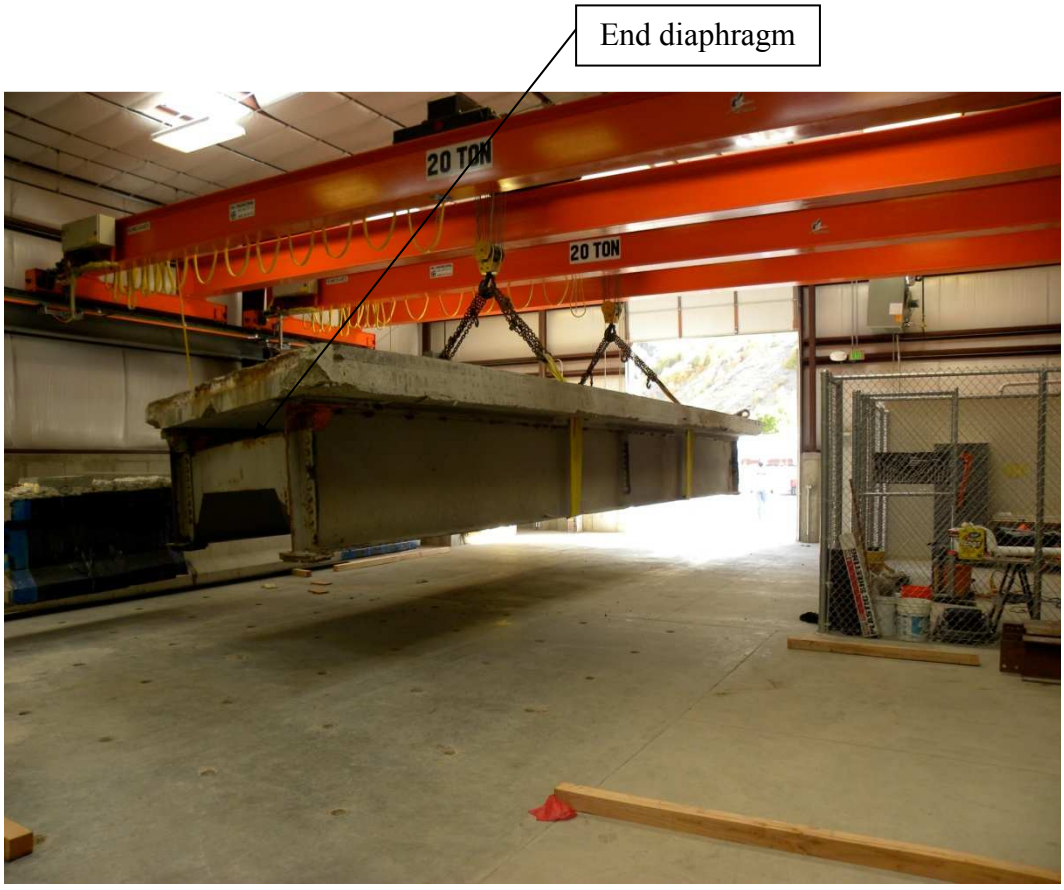

Figure 5. Bride Specimen 2 suspended in laboratory.

Flexural Tests

When using AASHTO LRFD Specifications for bridge design, it is necessary to predict the ultimate flexural capacity of individual girders, which encompasses post-elastic behavior. Cooperative research was focused on comparison of ultimate capacity to that predicted by AASHTO LRFD Specifications which prescribe the design of individual members (Cook, 2010). This dictated that the girders be individually loaded and failed. As a result, three flexural capacity tests were conducted.

Figure 6. Specimen 1 beneath reaction frame.

Experimental setup

All testing was performed at the USU Systems, Materials, and Structural Health (SMASH) Laboratory. The SMASH Lab houses a heavily reinforced concrete strong-floor, which is assumed to be rigid. The strong floor was used to anchor the base-plates of a movable steel reaction frame. The reaction frame consists of two vertical columns that support a horizontal reaction beam. The reaction beam has a heavily stiffened web. The test specimen was oriented beneath the reaction frame so that the reaction beam crossed directly over the centerline of the girder to be loaded as shown in Figure 6.

All instruments were monitored during the flexural tests with a Vishay Model 5100B Scanner data acquisition system. The experimental set up varied slightly between the tests for different reasons. Bridge Specimen 1 was supported at the ends of both girders (Reactions D1, D2, E1, and E2). The footprint at the base of each girder measured 254 mm (10.0 in.) by 203 mm (8.0 in.). The planes of the girder supports were nearly horizontal in the field; however, the 8th North Bridge had a super-elevation along its width and grade along its length. Therefore, the planes of the girder supports of the salvaged specimens were not parallel to the strong floor. Since this research was only interested in the vertical component of the reactions, spherical bearings were used to alter the load path from a non-vertical line to a vertical line. Various steel plates with a thickness of at least 51 mm (2 in.) were used between the girder flange support and spherical bearings. Each girder reaction was measured with a 1,780 kN (400^{k}) capacity foil strain gage based load cell, which was positioned beneath the spherical bearing. The load cells had inside and outside diameters of 76 mm (3.0 in.) and 150 mm (6.0 in.),

respectively. Various steel plates were used beneath the spherical bearings to accommodate the transverse super-elevation of the bridge sections.

These reactions did not account for any lateral translation of the girder supports. During testing of Bridge Specimen 1 it was noticed that the bridge system was deforming in the axial direction due to excessive plastic deformation of the steel girders. The support reactions remained at the same locations while the bottom flanges of the girders translated laterally above the reactions. This introduced eccentric loading of the load cells and was a large source of error in readings (Figure 7a). To mitigate this problem for Bridge Specimen 2, reactions were constructed which allowed for lateral movement (rollers). For one reaction, five steel cylinders measuring 51 mm (2.0 in.) in diameter were placed between the bottom steel plate and the strong floor (Figure 7b). This effectively created roller reactions, which allowed for longitudinal deformation. The rollers were placed at reactions B1 and C1.

a) b)

Figure 7. a) Eccentric loading of load cell and b) roller reaction.

String potentiometers (string-pots) were used to monitor the vertical deflection of the steel girders. For the testing of Bridge Specimen 1, three string-pots were used on Girders D and E at 0.25*L*, 0.5*L*, and 0.75*L* for a total of six deflection readings, where *L* is the overall length of the girder. The string-pots had a working range of 130 mm (5.0 in.). The string-pots were housed in a 305 mm (12 in.) long section of HSS203.2x101.6x6.4 (HSS4x8x1/4) for protection against falling concrete from destructive testing. Velcro was used to anchor the string-pots to the protective sleeve. A small hole was drilled into the HSS housing for the string to travel through. The end of the string was connected to a jack-chain. A small c-clamp was attached to the bottom flange of the girder, and the jack-chain was looped through the clamp and connected to itself with an 'S' hook (Figure 8a).

a) b)

Figure 8. a) Stationary and b) moveable string-pot setups.

During testing of Bridge Specimen 1 it was noticed that the steel girders experienced significant torsion resulting in large transverse displacements of the bottom flanges. Since the string-pots were stationary, their readings were not pure vertical deformation, but rather comprised by components of horizontal and vertical movement. To alleviate this problem for Bridge Specimen 2 a new string-pot set up was constructed. Two pieces of acrylic sheets measuring 6.4 mm (0.25 in.) thick were placed between the concrete and the protective HSS sections. Ten steel ball bearings with diameters of 6.4 mm (0.25 in.) were placed between the sheets of acrylic. This permitted the entire string-pot housing to translate in any lateral direction. A telescoping rod was connected to the steel girder and the string-pot housing (Figure 8b). The telescoping rod allowed for vertical movement but restrained relative lateral movement of the string-pot housing and the steel girder. This moveable string-pot system constrained the instruments directly beneath the girders at all times, and subsequent string-pot readings were pure vertical deflection (Figure 8b).

Four moveable set ups were constructed and used for the testing of Bridge Specimen 2: three on the loaded girder (Girder C) at 0.25L, 0.5L, and 0.75L, and one on the unloaded girder (Girder B) at 0.5L. An additional string-pot was used to measure the axial deformation of the girder system. The protective HSS section was positioned vertically at a distance of approximately 460 mm (18 in.) from the Girder C's roller reaction. The string-pot cable/jack chain was connected to a c-clamp which was fastened to the end of Girder C directly above the roller reaction.

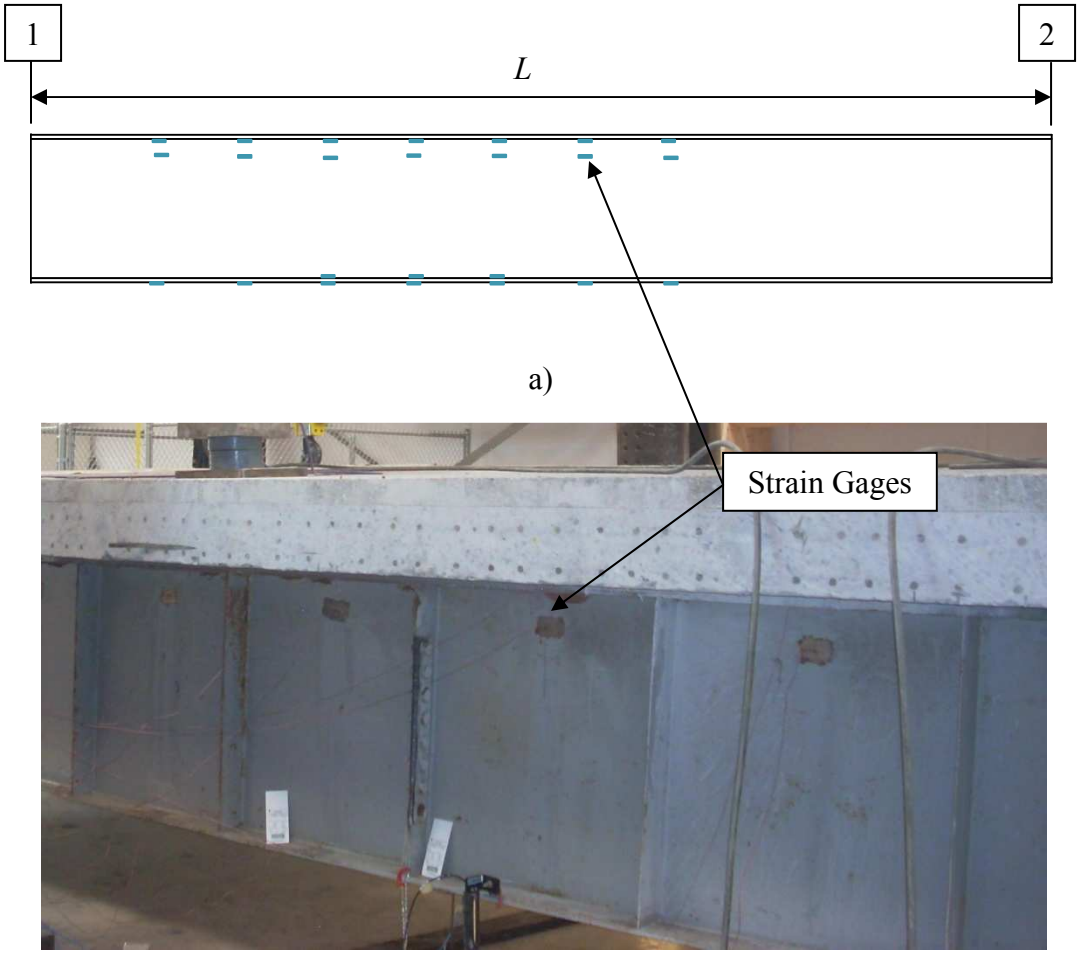

Figure 9. Loaded girder strain gage configuration a) for Specimen 2 and b) sample strain gages mounted to girder.

Uni-axial strain gages were mounted to the steel girders. There were two objectives of the strain gages: to monitor the neutral axis (N.A.) location and to map the region of plasticity in the girder throughout loading. The strain gages were attached to a prepared portion of the steel using a special bonding resin. The gages had a working range of approximately 15,000 microstrain (με). Approximately 20-25 gages were used during each flexural test at various locations of interest (Figure 9).

Testing procedure

A static point load was applied to the centerline of the loaded girder. The load was applied with a 5,340 kN (1200^{k}) capacity ram. The ram was placed between the reaction beam and the concrete deck of Specimen 1. A load cell was positioned beneath the ram monitor the load. A hydraulic pump supplied pressure to the ram (Figure 10b).

Since the concrete deck was super-elevated in the transverse direction, a spherical bearing was used between the deck and load cell. This corrected for the angle between the working line of the ram and the normal line of the concrete deck. Also, the spherical bearing prohibited eccentric loading of the load cell, which reduced error in readings. In some cases, various steel plates were used at the point load location to account for differences in elevation of the concrete deck in the transverse direction. The applied load was monitored with a load cell that matched the capacity of the ram (Figure 10a).

a)

b)

Figure 10. a) Ram, load cell, spherical bearing and b) hydraulic pump.

Table 1. Flexural tests description

Flexural Test	Bridge Specimen	Girder Loaded	Location of Point Load Along Girder
E	1	E	0.5*L*
D	1	D	0.5*L*
C	2	C	0.4*L*

The bridge specimens for this research project were subjected to three flexural tests (Table 1). During Flexural Test E, the loading was incremental to accommodate dynamic testing at various loading levels (see section: "Incremental Static/Dynamic Tests"). During Flexural Tests D and C, the loading was monotonic through failure. The bridge specimens were positioned so that the reaction beam was directly above the girder of interest at a specific longitudinal location.

In Flexural Tests E and D, the loading point was at 0.5*L* of the loaded girder in effort to produce a pure flexural failure. For Flexural Test C, the longitudinal loading location of 0.4*L* was chosen both because it coincided with the location of a transverse joint of the deck panels and because it was near mid-span. Also for Flexural Test C, the transverse diaphragm at mid-span was removed.

Results and discussion

One of the objectives of this research was to determine the degree of composite behavior exhibited by the precast panel decking system. This was accomplished by monitoring the N.A. of the system throughout flexural loading. It was assumed that plane sections remained plane throughout the bending test. Strain gages were mounted along

vertical planes at various locations along the length of the girder. The system curvature (i.e. differential strain divided by differential cross-sectional height) was calculated at each plane of strain gages. The curvature was used to interpolate the point of zero strain. Since no axial loads were present, the point of zero strain was taken to be the N.A.

The strain gage configuration best suited to monitor the N.A. throughout loading was during Flexural Test C (Figure 9b). The strain gages mounted on the bottom flange yielded first thereby making them useless to track the N.A. location. The strain gages mounted on the top flange and just beneath the top flange remained in the elastic region for a longer loading duration. This made it possible to interpolate the N.A. throughout the majority of loading. The theoretical elastic N.A. was calculated according to the transformed section method; it was determined to occur at a height of 963 mm (37.9 in.) measured from the bottom of the girder.

The N.A. locations for various cross-sectional planes along the length of the girder are plotted in Figure 11. In the elastic portion of loading, it can be seen that the measured neutral axis was higher than the centroid of the girder. This indicated that the decking system was contributing to flexural resistance. However, it is also shown that the N.A. was lower than the theoretically calculated elastic N.A. In other words, the decking system was not acting completely composite. In the post-elastic portion of loading, the N.A. shifts upward among cross-sectional planes of high moments (i.e. points close to 0.4L) as expected. Note that the strain gage data at 0.38L ends prematurely compared to the other gages. This was because these gages reached their working limit prior to ultimate loading.

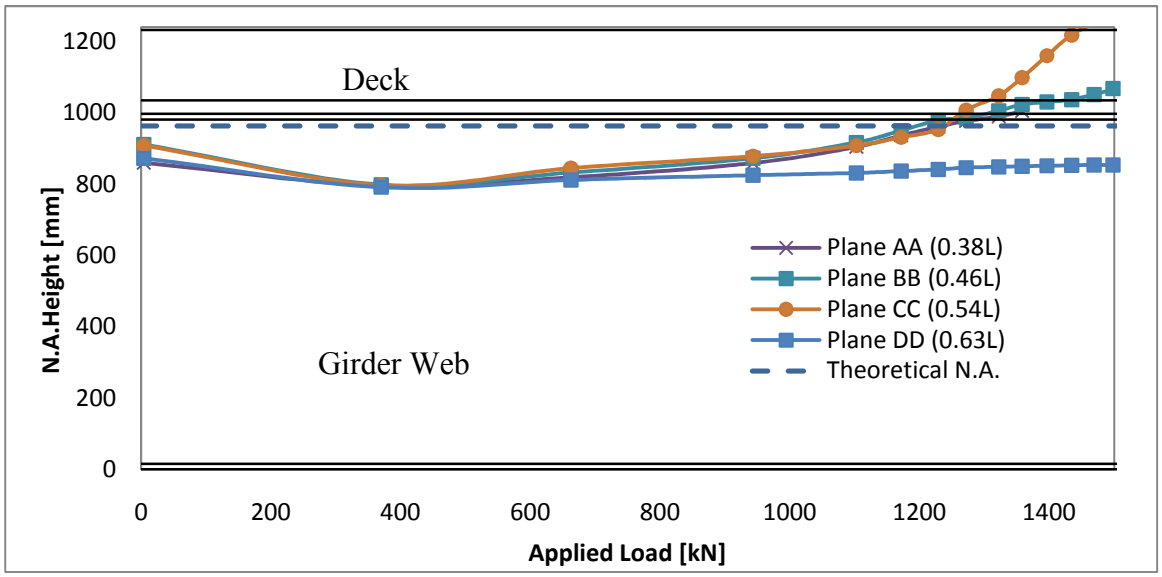

Figure 11. Flexural Test C N.A. locations.

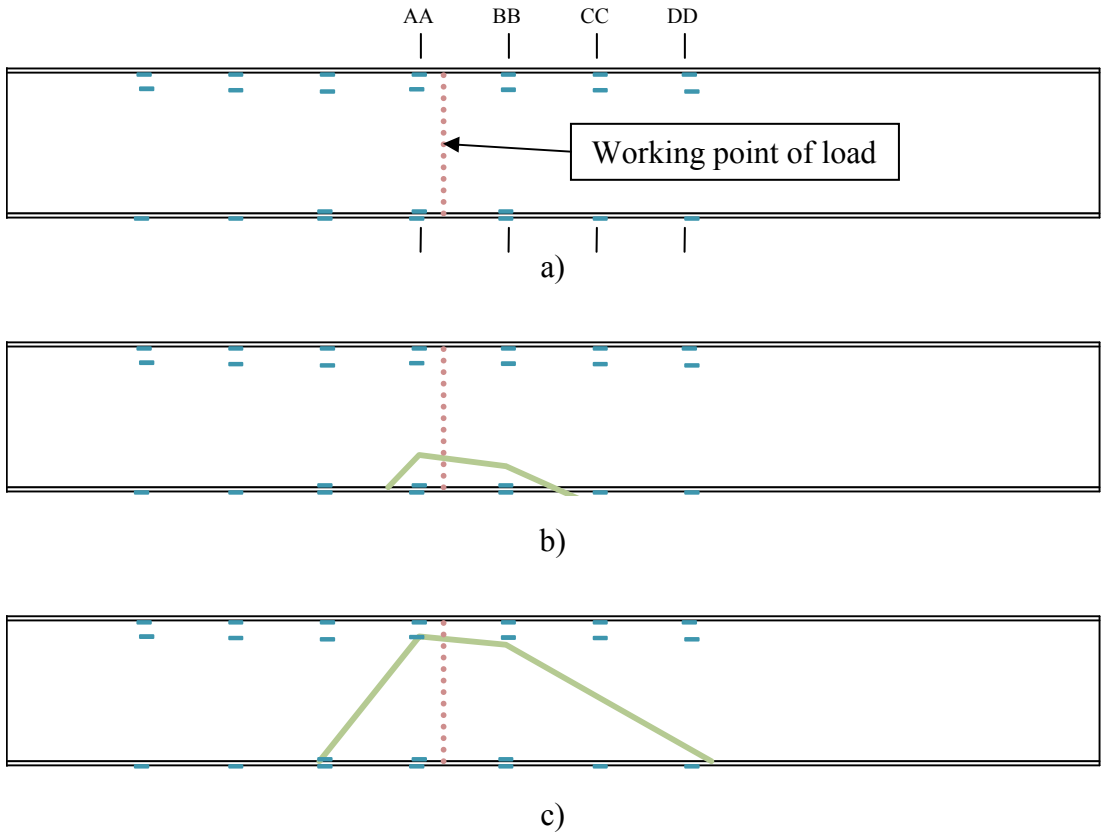

Figure 12. Flexural Test C plasticity region at a) 493 kN (111^{k}), b) 783 kN (176^{k}), and c) 1,020 kN (228^{k}).

The strain gage data was also used to map the region of plasticity at sequential loading points (Figure 12). This was done by extrapolating strains from the upper two gages to find the location of yield strain. The yield strain was determined experimentally to be approximately 1,300 με (see Chapter 4). The first recorded yield of the system was at a load of approximately 740 kN (170^{k}).

Deflections of the steel girders were measured at 0.5*L* on the loaded girder for all tests, among other locations. The mid-span deflections of the loaded girder are plotted in Figure 13. Because the loading points were not consistent between the tests (0.5*L* or 0.4*L*), the results are presented on a percent-of-maximum basis. The load-deflection curves for these two tests correlate very well.

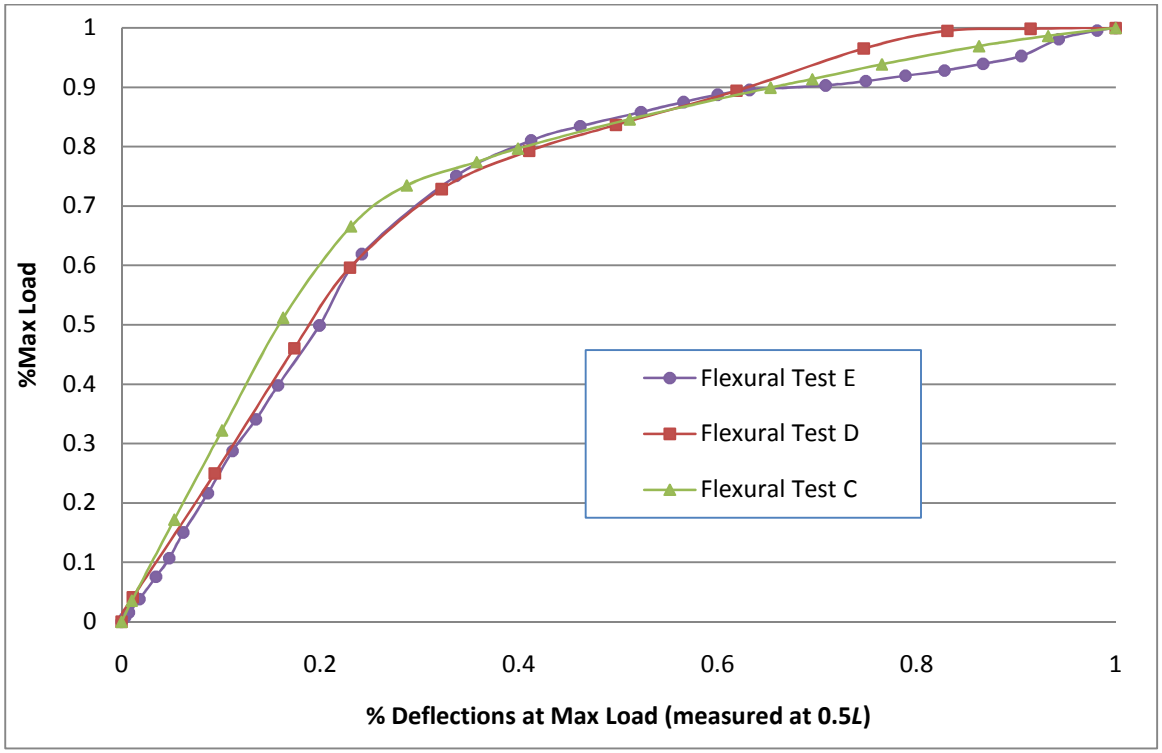

Figure 13: Load vs. deflection plots for flexural tests.

The data for Flexural Test C was assumed to be more accurate because of the improved instrument set up. It was noted that for Flexural Test C, the apparent yield load according to the deflection plot was approximately 1,100 kN (250^{k}). Also, for Flexural Test C at the time of maximum load, the mid-span deflection of the unloaded girder was 1.6% of the deflection measured on the loaded girder. This suggests that very little load was transferred to the unloaded girder.

The load cell readings at each reaction were divided by the total applied load to obtain the percentage of load distributed to that reaction. The results are plotted in Figure 14.

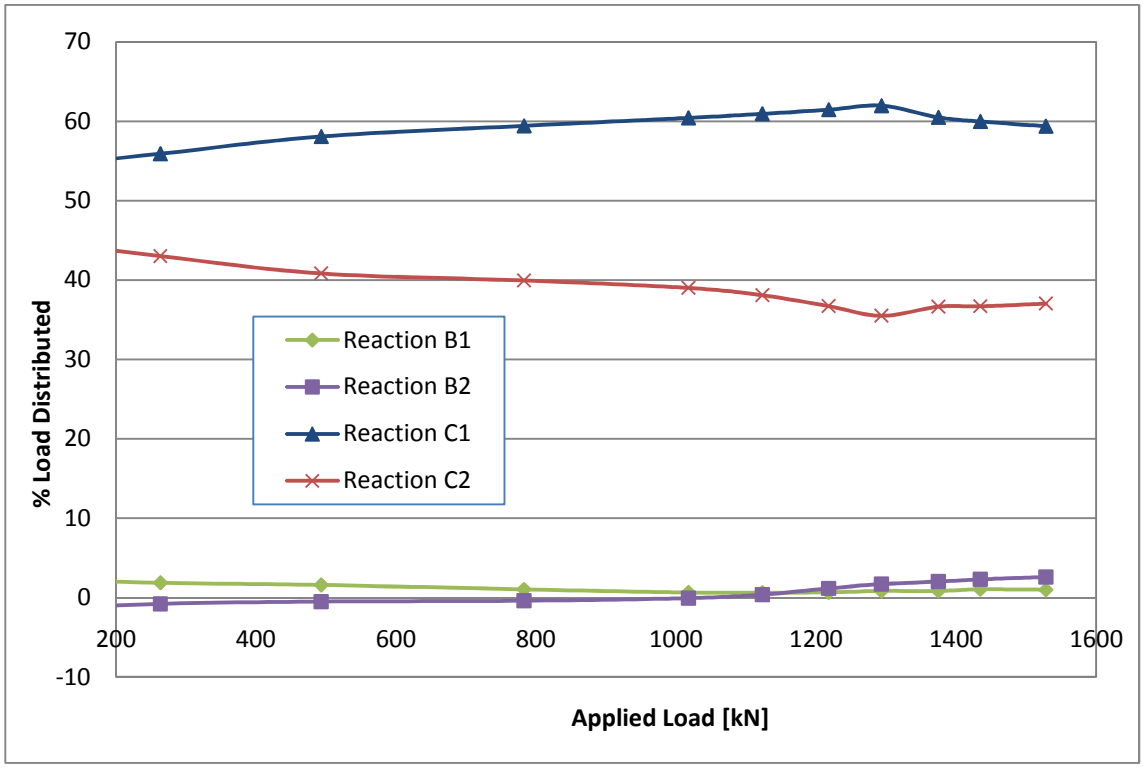

Figure 14. Load distribution for Flexural Test C.

There are several important observations that can be concluded from this graph. First, there was very little load distributed to the unloaded girder (Girder B). A maximum of 2.54% of the applied load was recorded at the unloaded girder reactions. This confirms the relatively low deflections of the unloaded girder. Second, the load distribution remains fairly constant throughout loading. There is a noticeable change in percent distribution at an applied load of about 1100 kN (250^{k}), which agrees with the apparent yield load in the load-deflection data. Lastly, beyond the yield load, there is very little deviation of percent load distributed among all reactions. A maximum 2.6% change in percent load distributed was recorded for Reaction C1.

All three flexural tests produced similar failure modes. The primary failure mechanism was large horizontal cracks in the concrete deck beneath the applied load. The cracks followed the top layer of longitudinal reinforcement indicating splitting failure in the concrete (Figure 15). As the load level increased, the cracks propagated longitudinally and expanded vertically. At the conclusion of the tests, the cracks opened up enough to expose longitudinal rebar that had buckled due to excessive compression.

This failure effectively eliminated the upper portion of the deck from moment resistance contribution. The deflections started to increase greatly. The load carrying capacity began to decrease as the concrete deck endured more damage. As the degree of deck damage increased, the system capacity began to converge to that of the steel girder alone. As a result, the loading became a function of the hydraulic pump flow rate because the girder was deflecting faster than the fluid could be pumped into the ram.

Figure 15. Splitting failure in concrete deck.

The splitting failure was likely introduced because of the salvaging process. The concrete cuts made in the field left only a 380 mm (15 in.) overhang distance of concrete (Figure 16). This is relatively small when compared to the 2,407 mm (94.75 in.) girder spacing. The smaller portion of overhang concrete introduced a non-symmetric section. Furthermore, the exact location of the cut produced an unknown clear cover distance of longitudinal reinforcement. The compressive reinforcement development length thus became the limiting factor in compressive concrete strength.

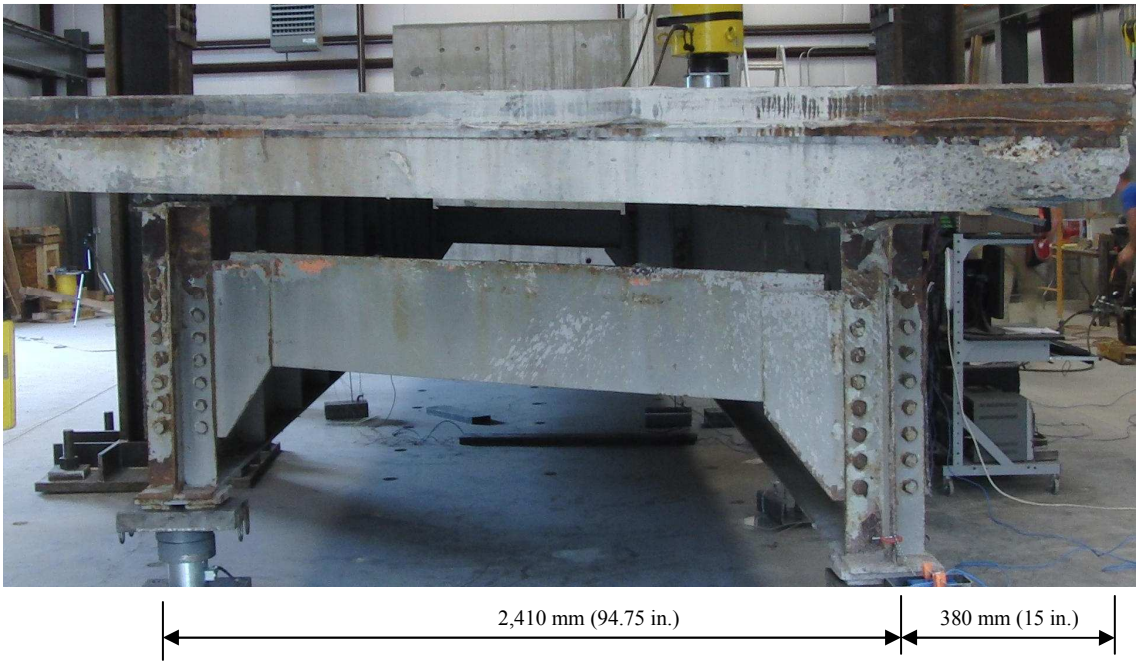

Figure 16. Transverse profile view of Specimen 2.

There was a secondary mode of failure that occurred after the splitting failure. After the top layer of concrete had been effectively removed due to splitting, the overall depth of concrete was reduced. This allowed for a localized punching shear failure to occur around the load. There was delamination and spalling on the underside of the deck. Since this is a secondary mode of failure, it is not as pertinent to this section as the primary splitting failure. The punching shear failure will be discussed in more detail later in the chapter where it is more prudent (see section: "Incremental Static/Dynamic Tests").

For Flexural Test C, video evidence revealed that the splitting failure initiated at a load of approximately 1,400 kN (315^{k}). At this load level, strain gages beneath the applied load indicated that the N.A. was located 1,020 mm (40.0 in.) measured from the

bottom of the girder flange. Also, the strain gages also recorded that the region of plasticity extended upward into the web a distance of 861 mm (33.9 in.). The equivalent stresses on the cross section at this load level are illustrated in Figure 17.

Using the Whitney stress block the uniform compressive stress, $0.85f_c$, acts across a width, *b*, and a depth, *a* (ACI, 2008). For the measured compressive strength of concrete (see Chapter 4) the distance, *a*, is equal to 65% of the neutral axis depth that is in compression, or 132 mm (5.20 in.). The width, *b*, was taken to be half of the entire bridge deck width, or 1,580 mm (63.0 in.), which included the overhang. The yield stress in the steel was determined experimentally to be 262 MPa (38 ksi) (see Chapter 4). In order to satisfy force equilibrium on the cross section the compressive stress in the concrete must be 19.7 MPa (2,850 psi). In other words, the splitting failure witnessed in the laboratory initiated when the concrete compressive stress reached this value.

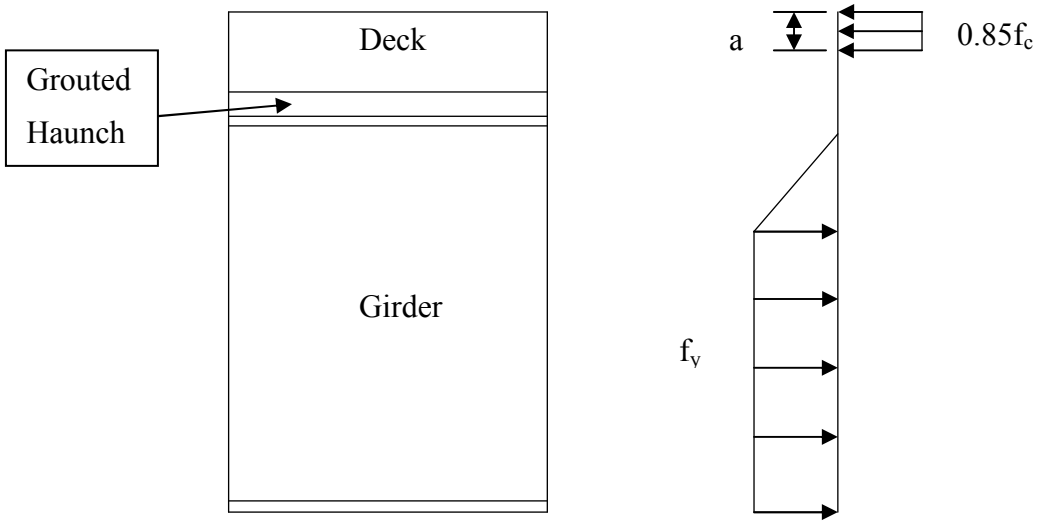

Figure 17. Flexural Test C stresses at 1400 kN (315k).

The ultimate load sustained for Flexural Test E was 1,490 kN (334^k). At the conclusion of the test, much of the deck beneath the applied load experienced severe cracking, splitting, and delamination. The damage extended towards the unloaded girder (Girder D). For the subsequent Flexural Test D, the ultimate load sustained was 1,330 kN (300^k). It is expected the damaged deck was the primary reason for the difference in ultimate capacities (greater than 10%) between these two tests. Nonetheless, both tests produced significant degrees of yield in the girders and similar splitting failures in the concrete deck.

The ultimate load sustained for Flexural Tests E and C was 1,560 kN (350^k). This is slightly greater than the ultimate capacity exhibited in Flexural Test E, which was expected because of the different loading locations. Using basic beam theory, a simple beam loaded at $0.4L$ would have a plastic load which is approximately 3.5% greater than the same beam loaded at $0.5L$. Applying this 3.5% increase to the ultimate load sustained in Flexural Test E yields a value of 1,540 kN (346^k), which is 1.1% lower than the ultimate load sustained in Flexural Test C.

Unfortunately, for all tests, the strain gages at the maximum applied loads were beyond their working range. Therefore, the researchers were unable to calculate a failure moment by the aforementioned section analysis method. However, the failure moment was approximated using another method. Since very little load was transferred to the unloaded girder, the system could be idealized as a two-dimensional statics problem. At the ultimate load, the reactionary forces were multiplied by their distance from the applied load to obtain a moment. Two moment values were calculated and averaged.

For Flexural Tests E and C, the failure moments were approximated as 4,140 kN-m (3,052 k-ft) and 3,910 kN-m (2,890 k-ft), respectively, which differ by 5.9%.

The final observation was that the loading of the transverse joint (Flexural Test C) had no apparent effect on overall compression deck behavior. This was evident because the loading of the transverse joint (Flexural Test C) produced very similar concrete deck damage as the loading away from the transverse joint (Flexural Tests E and D). The concrete cracks in Flexural Tests E and D were able to directly follow the top layer of longitudinal reinforcement beneath the applied load. The concrete cracks in Flexural Test C followed the top layer of reinforcement of one panel, the upper half of the transverse joint key, and the top layer of reinforcement of the adjacent panel, despite the fact that the reinforcement was discontinuous at the transverse joint key (Figure 18).

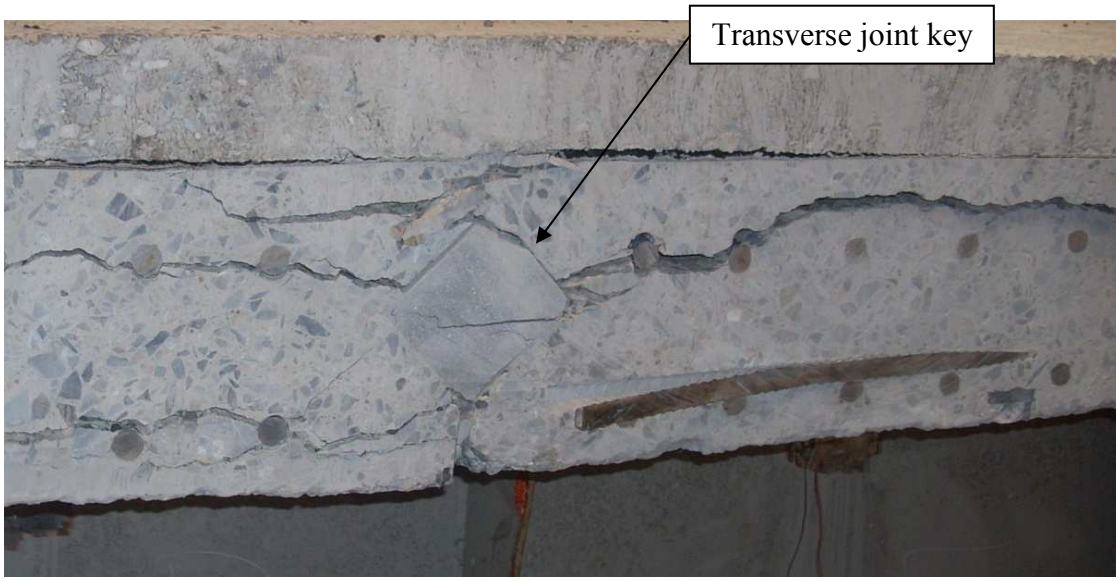

Figure 18. Splitting failure through transverse joint key.

Beam Shear Tests

An important failure mode considered in the design of bridges is beam shear. Bridge Specimen 2 was subjected to two beam shear tests. As with the flexural tests, cooperative research dictated that individual girders be loaded and failed.

Experimental setup

All instruments were monitored during the beam shear tests with a Vishay data acquisition system. A load cell was place directly beneath a hydraulic ram to record changes in the applied load. The four reactions (C1, C2, B1, and B2) were constructed and monitored with load cells as well. To prevent eccentric loading, roller reactions used in the flexural tests were implemented (Figure 7b).

String-pots were attached to the girder as shown in Figure 8b at predetermined locations. For the loaded girder, string-pots were positioned at quarter and half points as well as directly beneath the applied load. For the unloaded girder, a string-pot was placed at mid-span.

Various strain gages were attached to the girder webs near the predicted shear failure. The orientation and locations of these gages were at particular points of interest to monitor any post-buckling tension struts. Twenty-five and 26 strain gages were used for Beam Shear Test B and C, respectively (Figure 19).

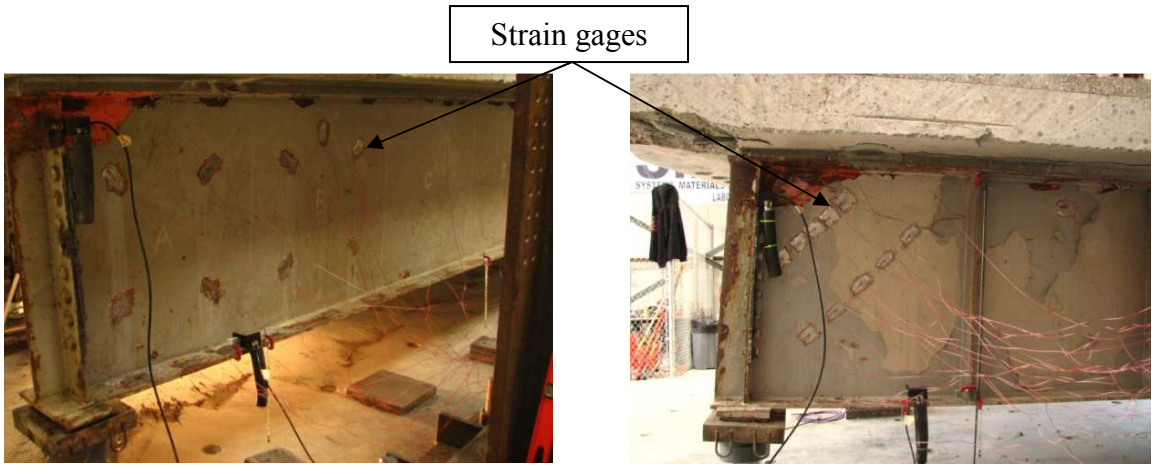

a) b)

Figure 19. Strain gage configuration for Beam Shear Tests a) B and b) c.

Testing procedure

Bridge Specimen 2 was loaded at specific locations to produce beam shear failure modes. For each beam shear test, a point load was applied directly above a girder at a predetermined location which was slightly greater than *d* away from the nearest reaction, where *d* is the overall depth of the system. The overall depth of the 8th North Bridge was 1.23 meters (48.5 in.). Accordingly, Bridge Specimen 2 was positioned beneath the reaction frame so that point loads were applied a distance of approximately 1.3 m (51 in.) away from the nearest reaction. Two beam shear failure tests were conducted (Table 2). A point load was applied with a hydraulic ram at the specified location to produce the beam shear failure (Figure 20). The loading was applied monotonically until failure for both tests.

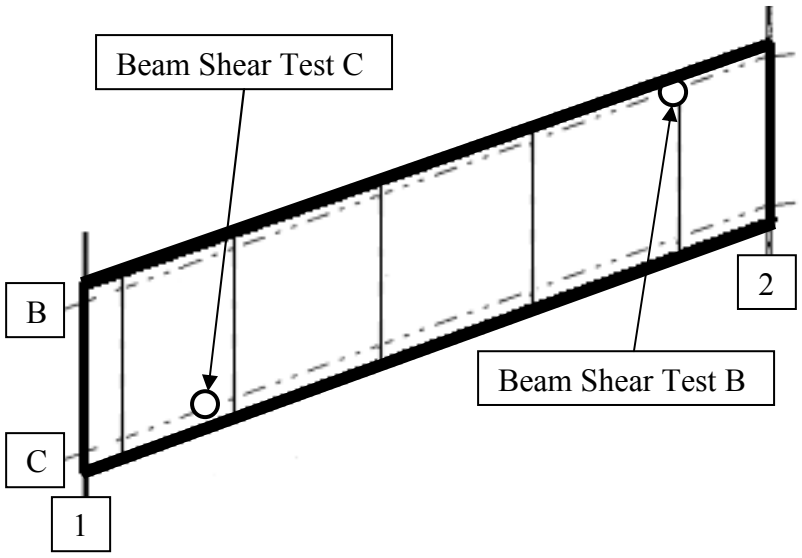

Figure 20. Locations of beam shear tests.

Table 2. Beam shear tests description

Beam Shear Test	Bridge Specimen	Girder Loaded	Load Location
C	2	C	0.12*L*
B	2	B	0.88*L*

A secondary objective of the beam shear tests was to investigate the effects of loading of the transverse joint connections. As shown in Figure 20, the load was applied directly over a transverse joint for Beam Shear Test B. For Beam Shear Test C, the load was applied away from the transverse joint.

Results and discussion

The magnitudes and modes of failures from both beam shear tests were extremely consistent. In both cases, there were two obvious signs of shear failure: post-buckling

tension-struts of the steel girder and large diagonal cracks in the concrete deck (Figure 21). Various plastic hinges developed in the girder including: two in the top flange near the strut, one in the web stiffener above the reaction, and one in the bottom flange at the base of the tension-strut. In both tests, the large diagonal crack in the concrete deck extended transversely through the concrete deck but did not extend completely to the unloaded girder. For Beam Shear Test B, there was no visible damage to the transverse joint, despite the fact that the load was applied directly to the joint.

The maximum shear forces sustained during the tests were taken directly from the nearest load cell reading. Beam Shear Tests B and C had maximum recorded shear capacities of 1,340 kN (301^{k}) and 1, 1,240 kN (278^{k}), respectively. This corresponds to a difference in shear capacity of 8.3% between the two tests.

Figure 21. Beam Shear Test B failure.

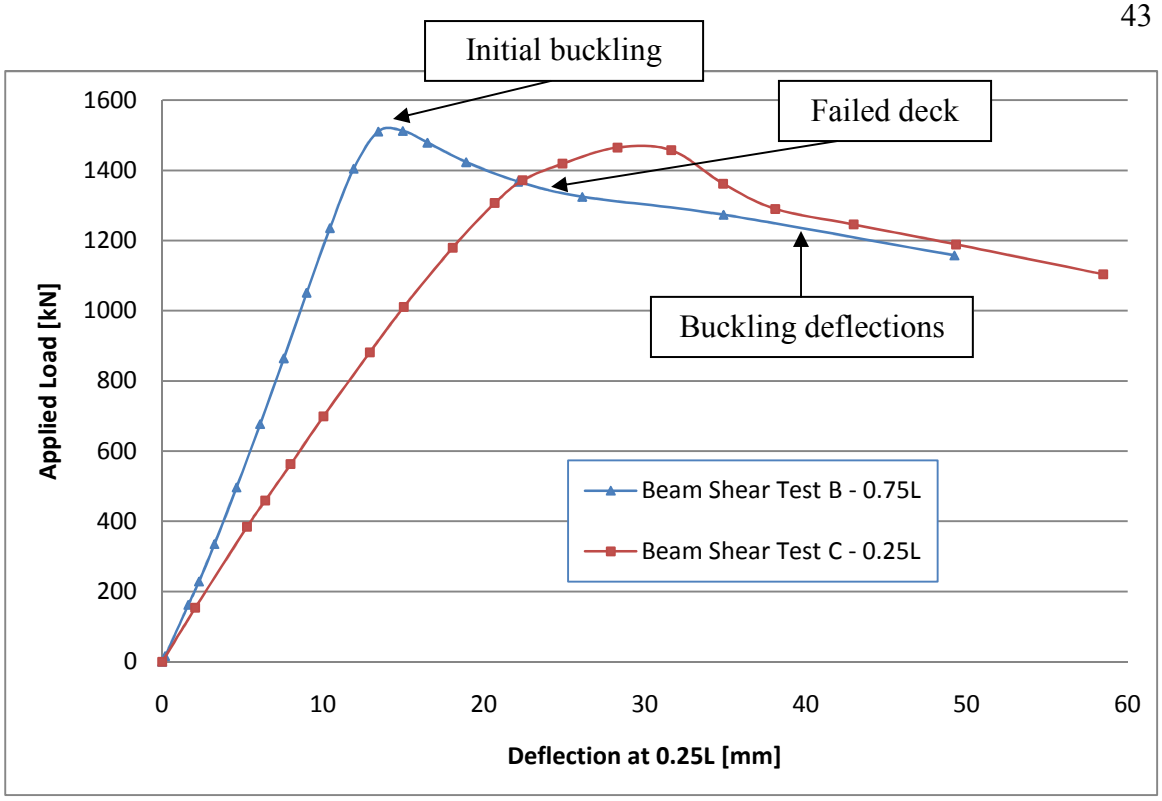

Figure 22. Load vs. deflection at 1/4 points for beam shear tests.

The sequence of damage inflicted to the system during the beam shear tests is very important to the load-carrying capacity of the system. For illustration, the damage progression will be related to the load-deflection plot shown in Figure 22. The deflections shown in this plot are at the quarter point nearest to the loaded reaction.

There is a discrepancy between the load-deflection plots of the two beam shear tests. Deflection readings were approximately 17 mm (0.7 in.) higher during Beam Shear Test C. This is likely due to the initial damaged state of Bridge Specimen 2. The testing order on this bridge specimen was Beam Shear Test B, Flexural Test C, and Beam Shear Test C. Flexural Test C was conducted on the same girder (Girder C) as Beam Shear Test C. Due to excessive splitting failure of the reinforced concrete, much composite

action was likely eliminated at this location. The reduced section stiffness of Girder C was the probable cause of the higher deflections measured during Beam Shear Test C. The system damage caused by the flexural test was largely isolated towards the center of the girder while the deck near the support was undamaged; therefore, the shear capacity between the two tests exhibited less discrepancy than the load-deflection plots.

Since damage was a pre-existing factor in Beam Shear Test C this research will focus on data from Beam Shear Test B. The deflection curve can be idealized into three linear portions: an elastic region, a concrete-failure region, and a plastic region. The system remains nearly elastic until the maximum load. Very near the time of maximum load, the first yield among all strain gages was recorded. These strain gages were oriented along the diagonal post-tension strut in between the first and second web stiffeners at the loaded reaction (Figure 19). This indicates the first step in web buckling. Video was recorded during the failure test. Visual damage from the video was directly correlated to the magnitude of applied load. The first apparent buckling strut can be seen at approximately 97% of the maximum load *after* the maximum load had been sustained. This buckling strut grows in out-of-plane amplitude for the remainder of the test.

The second linear portion of the deflection curve corresponds to the deck failure. The failure of the concrete deck can be separated into two steps. First, at approximately 94% of the maximum load after the maximum load had been sustained, the diagonal crack in the concrete is visible. There was no sound of this crack recorded on the video. It was suspected that this crack would have been apparent in the deflection data; however, it wasn't. It is believed that once the steel girder had deflected enough to

mobilize the shear contribution of the concrete, the applied shear was well above the capacity of the deck. This instantly produced the concrete cracking failure, while the majority of shear was still being carried by the girder.

The second step in the deck failure occurs at approximately 91% of the maximum load after the maximum load was sustained. There was a de-bonding failure of the grouted shear pocket connecting the girder to the deck. This shear pocket was directly above the loaded reaction. The shear studs remained connected to the top flange, and the grout remained bonded to the shear studs. The failure was at the grout/concrete interface. The mass of grout pulled away from the pocket in the deck panel (Figure 23).

Figure 23. Grouted shear pocket failure.

The third linear portion of the deflection curve represents pure buckling deflections of the girder. In this region the concrete deck had failed in shear as well as de-bonded from the nelson shear studs. Therefore, at this point, the concrete contributed very little to the system capacity. From this point on the load carrying capacity of the girder decreases linearly and the deflections of the system continue to increase. The reason that deflections increase with decreasing load is because of the mode of deformation. Rather than strain-hardening, in which case the system strength would increase, the system is buckling. The increased degree of buckling directly relates to a lower load carrying capacity. At the time of test termination, which was well beyond the maximum applied load, the system was deforming at the same slope of the plastic region of deflection.

After the failure of Beam Shear Test 1 the condition of the steel girder was inspected. It was discovered that the web stiffeners along both girders were in fact not welded to the bottom flange. Figure 24 shows the displacement of the stiffener nearest to the loaded reaction in Beam Shear Test B. The original position of the stiffener can easily be determined by the peeling of paint at the joint. It was concluded that the un-welded bottom flange connection likely had an effect on the shear-buckling capacity of the system. The other stiffeners were inspected. It was found that the stiffeners directly above supports and at mid-span of both girders were completely welded to the girder; all other stiffeners were only welded to the top flange and web.

Figure 24. Web stiffener displacement after Beam Shear Test B.

Punching Shear Tests

The final failure mode investigated for this research was punching shear of the precast deck panels. Specifically the transverse joints were the area of focus. Four tests were conducted to determine the effects of transverse joints on punching shear capacity.

Experimental setup

The only instruments used during the punching shear tests were load cells, which were monitored with a Vishay data acquisition system. A load cell was place directly beneath a hydraulic ram to monitor the applied load. All four reactions were constructed and monitored with load cells. No deflections, strains, or rotations were measured during the punching shear tests.

Table 3. Punching shear tests description

Punching Shear Test	Bridge Specimen	Load at Transverse Joint
1	1	Yes
2	1	No
3	2	Yes
4	2	No

To isolate the effects of transverse joints on punching shear capacity it was necessary to conduct four tests (Table 3). For Punching Shear Tests 1 and 3 a point load was applied directly over or very near a transverse joint in the deck system. For Punching Shear Tests 2 and 4 a point load was applied towards the center of the panel where no transverse joints existed in the region of punching shear. In all cases, the point loads were applied directly between or very near the middle of the girder centerlines. This was done to ensure a punching shear failure of the deck panels only. Prior to all tests an area of asphalt was removed from the concrete deck. This area was approximately 460 mm by 460 mm (18 in. by 18 in.).

Testing procedure

Four punching shear tests were performed on the two bridge specimens. A point load was applied with a hydraulic ram at strategic locations (Figure 25). Previous flexural and shear tests caused localized damage to the bridge deck, and therefore the locations were also based on the condition of the deck panels. The loading was monotonic for all tests throughout failure.

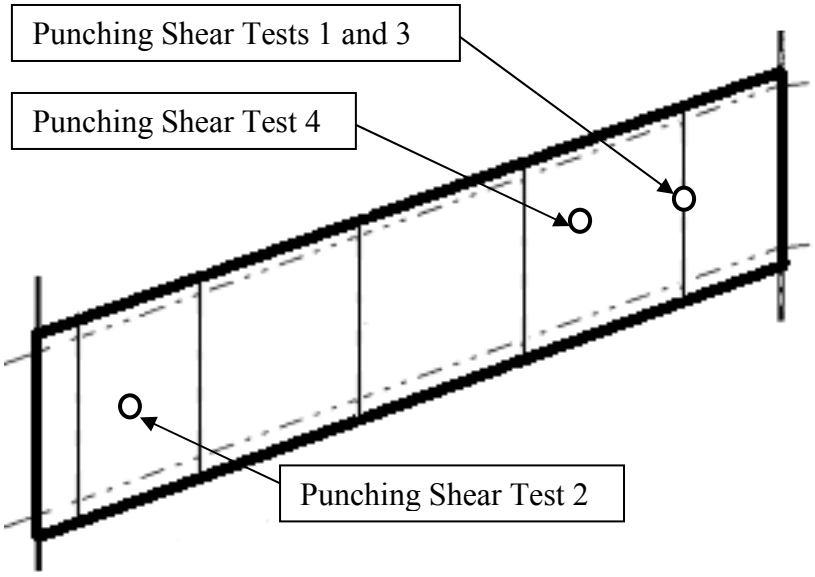

Figure 25. Locations of punching shear tests.

Results and discussion

Two types of failures were experienced. For Punching Shear Tests 2 and 4 a classic punching failure was observed. The concrete deck fractured along a diagonal plane radiating out from the load point. The resulting damage was a cone-shaped shear failure surface. The reinforcement suspended much of the crumbled concrete although its structural capacity was lost. Much of the concrete surrounding the base of the cone spalled off exposing the bottom layer of reinforcement in the panels (Figure 26).

Figure 26. Underside of deck after Punching Shear Test 2 failure.

The loading location of these two tests most closely represented that of a continuous deck. Therefore, this type of failure was considered the control for the experiment. Punching Shear Tests 2 and 4 yielded ultimate capacities of 623 kN (140^{k}) and 810 kN (182^{k}), respectively.

The second type of failure observed was during Punching Shear Tests 1 and 3. These tests consisted of loading on the transverse panel joints. The primary components connecting the panels across the joint were welded studs embedded into the side of the panel (Figure 3). There were five of these connections across the length of the joint which were equally spaced throughout the girder spacing. The secondary connecting

mechanism was the bond and mechanical bearing at the concrete-grout interface of the shear key.

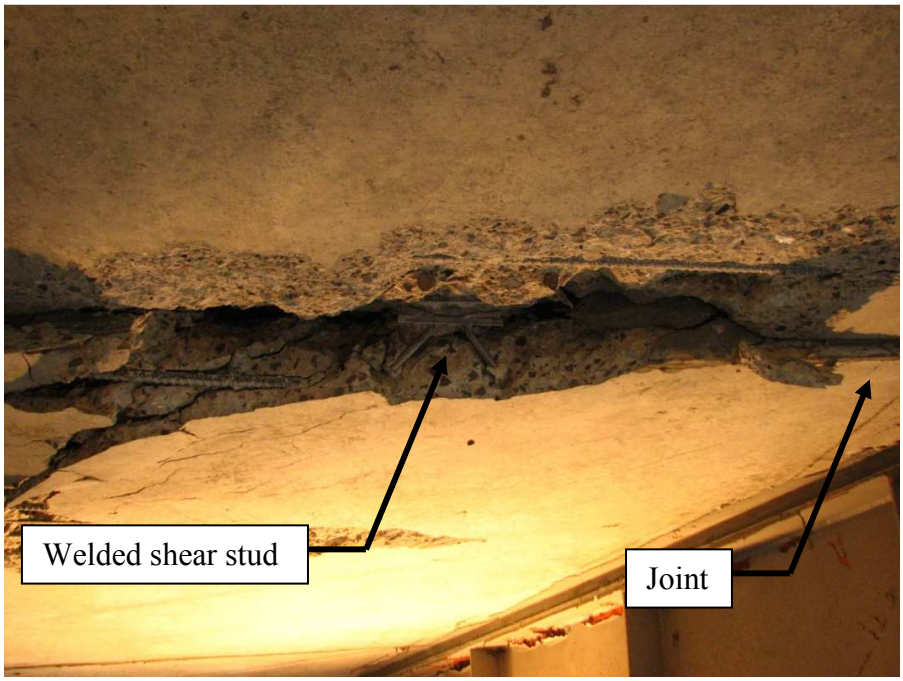

Figure 27. Underside of deck after Punching Shear Test 3 failure.

The transverse joint was the variable of interest in the experiment. During these two tests the load was applied over a welded stud shear key. The majority of the deck damage was isolated to the transverse joint. The failure surface surrounded the shear key in a somewhat conical fashion. In both cases, the shear keys were easily excised from the specimen. An exposed shear key can be seen in the middle of Figure 27. There was cracking and spalling of concrete on the underside of the panels along the joint. Away from the joint there were visible hairline cracks on the underside of the deck, although the panels appeared to be in good condition. There was also de-bonding of the

grout/concrete interface throughout the joint (Figure 27). Punching Shear Tests 1 and 3 yielded ultimate capacities of 372 kN (83.7^{k}) and 404 kN (90.9^{k}), respectively.

The ultimate capacities of like tests were averaged. For the continuous panel test, there was an average ultimate capacity of 717 kN (161^{k}). For the transverse joint test, there was an average ultimate capacity of 388 kN (76.0^{k}). In other words, the transverse joint tests yielded ultimate capacities that were 46% lower than the continuous panel tests.

Incremental Static/Dynamic Tests

One objective of this research was to investigate the effects of damage on dynamic behavior. Theoretically, plastic deformation of a structural member has an effect on member stiffness and hence dynamic response. This relationship was examined by subjecting Bridge Specimen 1 to incremental flexural loads and monitoring the changes in dynamic response at each load level.

Experimental setup

To obtain natural frequencies and mode shapes of the bridge system, velocity transducers were mounted to the concrete deck. A total of fourteen transducers were used: ten vertical sensors and four horizontal sensors. Half of the sensors were positioned directly above the North Girder and the other half were positioned directly above the South Girder. On either girder, five vertical sensors were mounted at 0.14L, 0.39L, 0.61L, 0.77L, and 0.91L, where L is the overall girder length. On both girders, two

horizontal sensors were mounted at 0.40*L* and 0.62*L* (Figure 28b). All sensors were connected to a Data Physics Signal Processor.

The Data Physics system was connected to a Personal Computer (PC) using a local area network (LAN) connection. The data acquisition system was controlled by the SignalCalc software package. Excitation of the bridge system was provided using a 444.8 N (100 lb) shaking device oriented vertically on the deck. The shaking device was positioned at a location which did not coincide with any expected nodes of lower-range modes (Figure 28). This location was approximately 0.73*L* along Girder E and approximately 0.86 meters (2 ft 10 in.) towards Girder D. The excitation signal was generated by the Data Physics system. The signal was amplified using an external signal amplifier. A swept-sine excitation signal was chosen for this testing. Using this signal, the shaker device commences oscillation at an initial frequency and gradually increases until a final frequency is reached. The process is then repeated in reverse to complete one sweep. The initial and final frequencies were set to 3 Hz and 50 Hz, respectively.

While the swept-sine signal is convenient to set up and implement, the drawback is that the shaker frequency is constantly changing, which ultimately introduces noise into the output signals. When the excitation signal passes through resonance, large magnitudes of vibrations are induced which take time to completely dampen out. As the excitation signal passes just outside of a resonance frequency, the velocity transducers may still be recording high resonant vibrations that haven't fully ceased. This problem can be mitigated two ways. First, the duration of one complete sweep can be lengthened to allow sufficient time for resonant vibrations to dampen out. Second, multiple sweeps

can be recorded and averaged to ensure that any noise can be cancelled out from sweep to sweep. Both of these methods were attempted and final excitation signal settings were determined by an iterative process. During this testing, 128 seconds were given to complete one sweep, and 10 sweeps were used to compute an average output signal at each load increment.

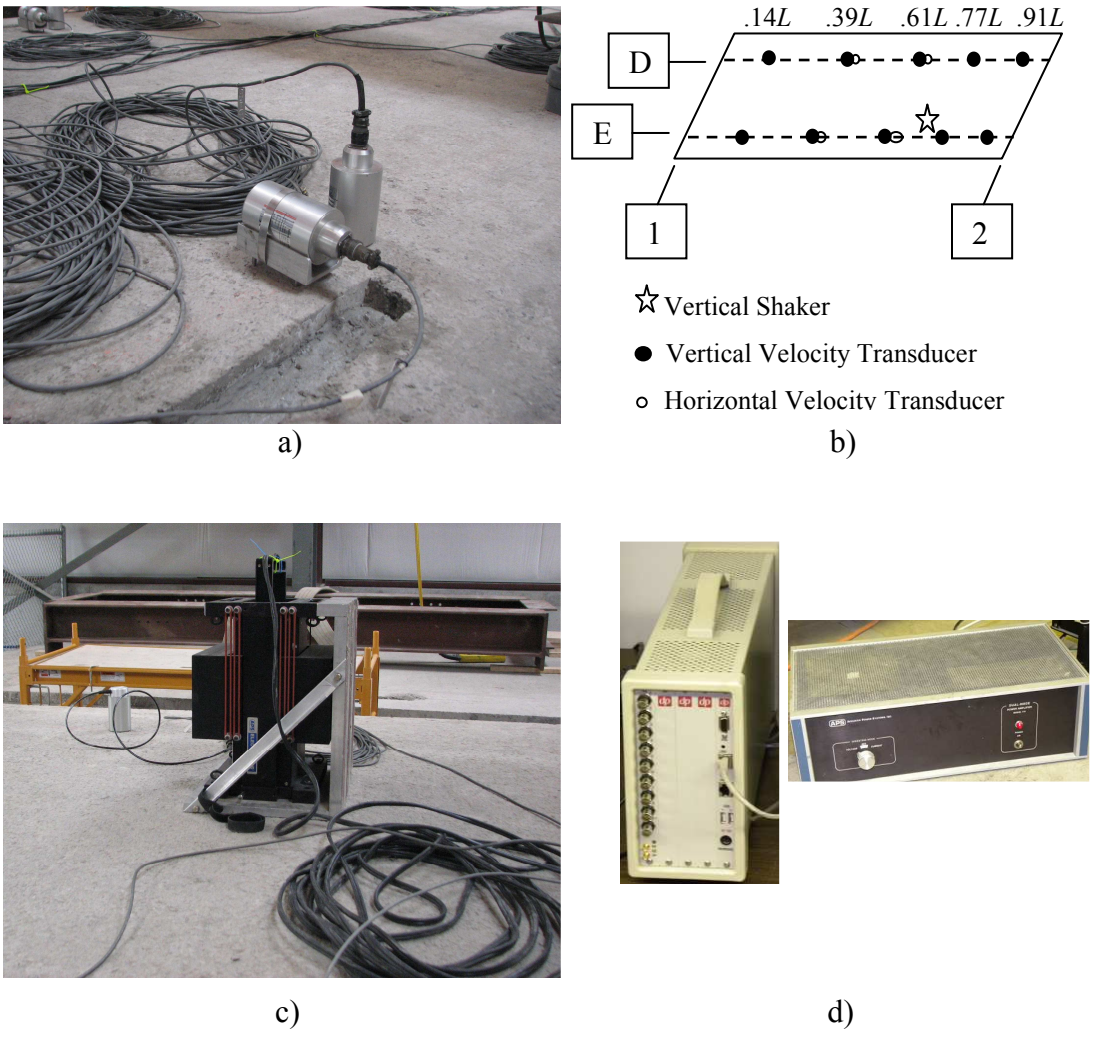

Figure 28. Dynamic equipment setup: a) velocity transducers, b) transducer layout, c) vertical shaking device, and d) Data Physics data acquisition system.

Signal processing

The Data Physics Signal Processor recorded the velocity-time data from the sensors. This data was subjected to a Hanning window, which filtered out data at the beginning and ending of the time spectrum that was expected to be inaccurate. The software then performed a fast Fourier transform (FFT) to convert the time data into the frequency domain which was used to obtain a Frequency Response Function (FRF). The FFT algorithm involves separating the output signal into individual sine waves which comprise the overall signal. The amplitudes and frequencies of individual sine waves are plotted to transform the signal from the time domain to the frequency domain. The FRF was computed by dividing the FFT output signal by the FFT excitation signal, which results in a complex equation. The equation was broken down to develop the magnitude and phase of the FRF. The magnitude of the FRF was calculated by taking the square root of the sum of the squares of the real and imaginary components of the FRF. The phase is calculated as the ratio of the imaginary component to the real component of the FRF (Data Physics Corporation, 2006).

The Data Physics Signal Processor software also calculates a Coherence Function, which is a measure of quality of data that ranges from zero to one. A Coherence of one indicates that the input signal is completely causing the output response. Alternatively, a Coherence of zero indicates that the output response is independent of the input signal (Data Physics Corporation, 2006).

Table 4. Dynamic test description

Dynamic Test	Testing Day	Previous Static Load Reached kN (k)
1	1	359 (80.7)
2	1	445 (100)
3	1	544 (122)
4	1	625 (141)
5	1	715 (161)
6	1	812 (183)
7	1	901 (203)
8	2	988 (222)
9	2	1,070 (241)
10	2	1,160 (261)
11	2	1,250 (280)
12	2	1,330 (299)
13	3	1,310 (294)
14	3	1,420 (320)
15	3	1,490 (335)

Testing procedure

For each load increment the maximum load was sustained for approximately 30 seconds. The pressure supplied by the pump gradually decreased with time; however the applied load only varied within 3% of the maximum load throughout the duration of loading. After the load was removed, the dynamic test was conducted. Natural frequencies and mode shapes were computed using the measured response recorded by the Data Physics system. After the dynamic measurements, the static point load was reapplied and increased by approximately 89.0 kN (20.0^{k}) each test. A total of fifteen dynamic tests were completed at increments until failure of the bridge section (Table 4). The entire dynamic testing was conducted over a three-day period.

Results and discussion

The Data Physics system collected and processed the output signals from the velocity transducers during the dynamic tests. The software generated a FRF consisting of Magnitude and Phase Plots and a corresponding Coherence Function. These plots for the vertical sensors for Dynamic Test 1 are shown in Figure 29. Note that Sensor 10

(located on Girder D) generated nearly zero magnitude, a phase plot that is not consistent with any of the other nine sensors, and a relatively poor coherence. These three observations indicated that Sensor 10 was malfunctioning. Consequently, the data recorded by this sensor will be disregarded for the remainder of this research.

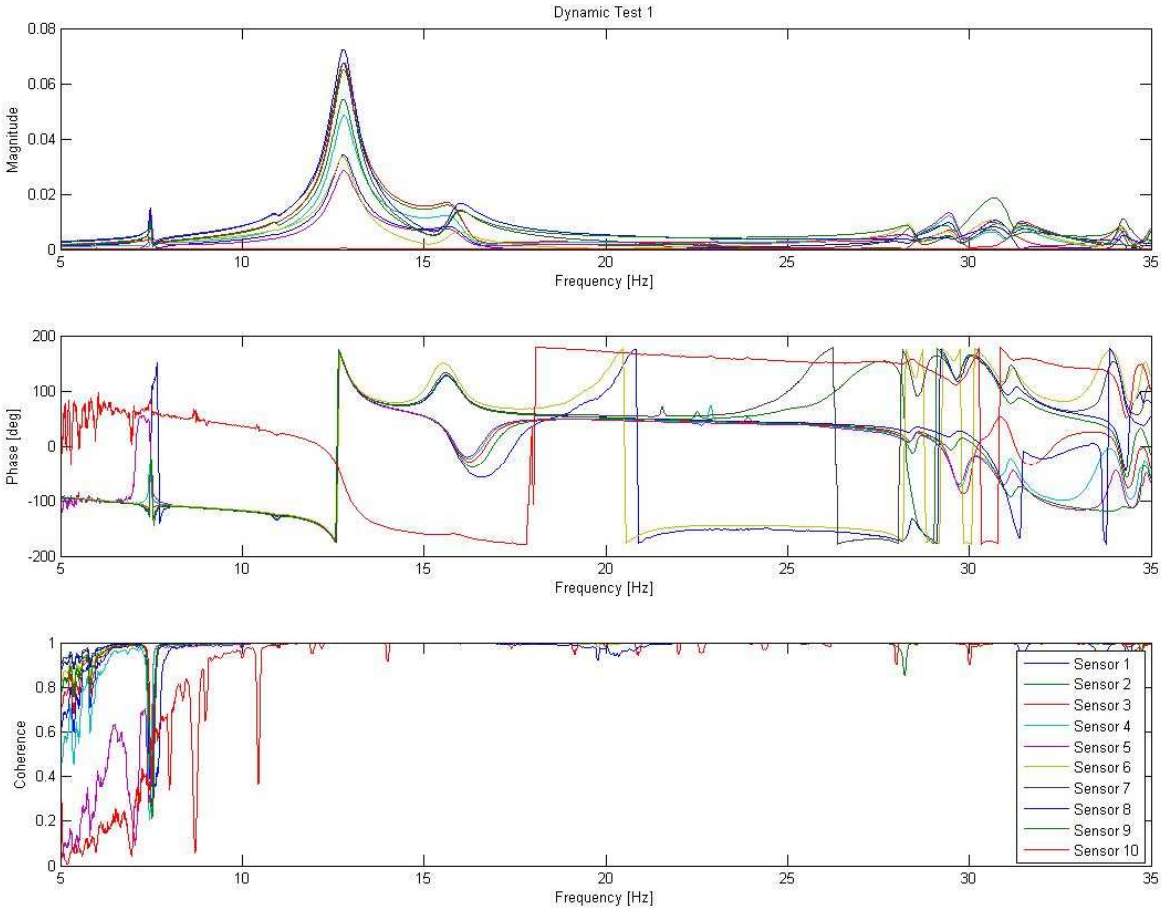

Figure 29. Dynamic Test 1 FRF, Phase Plot, and Coherence Function.

Also, the horizontal sensors generated a response of approximately 2 to 5% of the magnitude output as the vertical sensors. This is as expected because the shaker was oriented vertically during the test. Therefore, the horizontal sensors will also be further disregarded.

Using these plots, resonance was be defined by using three criteria. First, a localized maximum must be exhibited by all sensors on the magnitude plot. The frequencies of individual peaks were averaged to obtain the possible natural frequency. Secondly, the phase plot was inspected at the frequency of the localized maximum. The sensors at that frequency were required to be in phase or out of phase by 180 degrees. Lastly, all sensors were required to demonstrate high coherence at the frequency of the localized maximum. Coherence values below 0.9 indicate poor sensor response and were examined with caution. When a localized maximum on the magnitude plot met these criteria, it was considered resonance. When a natural frequency is encountered, the approximate mode shape was plotted. Relative displacements of the sensors were calculated by their relative magnitudes at the natural frequency. The phase plots were then examined to determine which sensors were in phase (i.e. plotted as positive displacement) and which sensors were out of phase (i.e. plotted as negative displacement).

The first resonance occurred at 12.79 Hz. This is the predominant mode of the bridge system because of its relative amplitude in relation to the rest of the spectrum. All sensors were found to be in phase at this frequency and showed coherences very close to one, indicating quality data. This resonance will further be designated as Mode 1.

The next possible resonance occurs in the range of 15.64 to 16.01 Hz. It appeared that two peaks existed, though they were near the same frequency. Further examination revealed that the two peaks are formed by sensors of like girders (Figure 30). The phase plots show that the sensors of like girders were in phase. Sensors of unlike girders were not quite 180 degrees out of phase, but they were certainly not in phase. This indicates a torsional mode that was somewhat "smeared" through a range of frequencies. This could possibly be caused by the skew angle of the bridge. This resonance will be further designated as Mode 2. Natural frequencies of this mode will be reported as a range of possible frequencies.

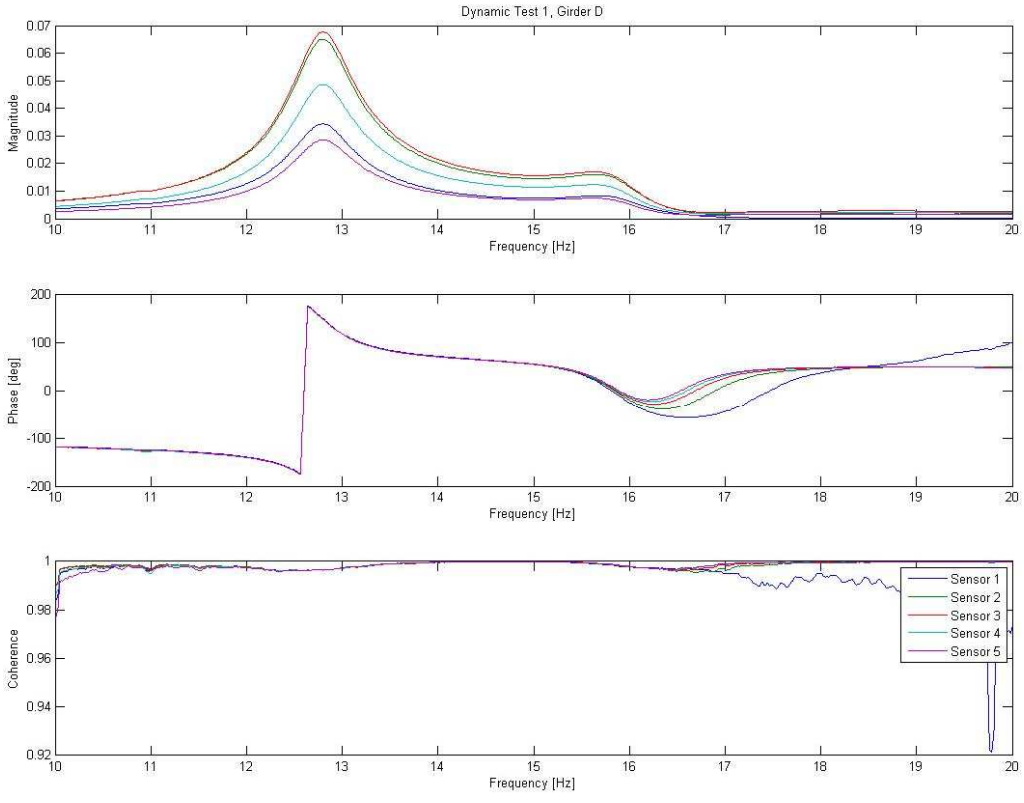

a)

Figure 30. Dynamic Test 1 FRF, 10-20 Hz, for a) Girder D and b) Girder E.

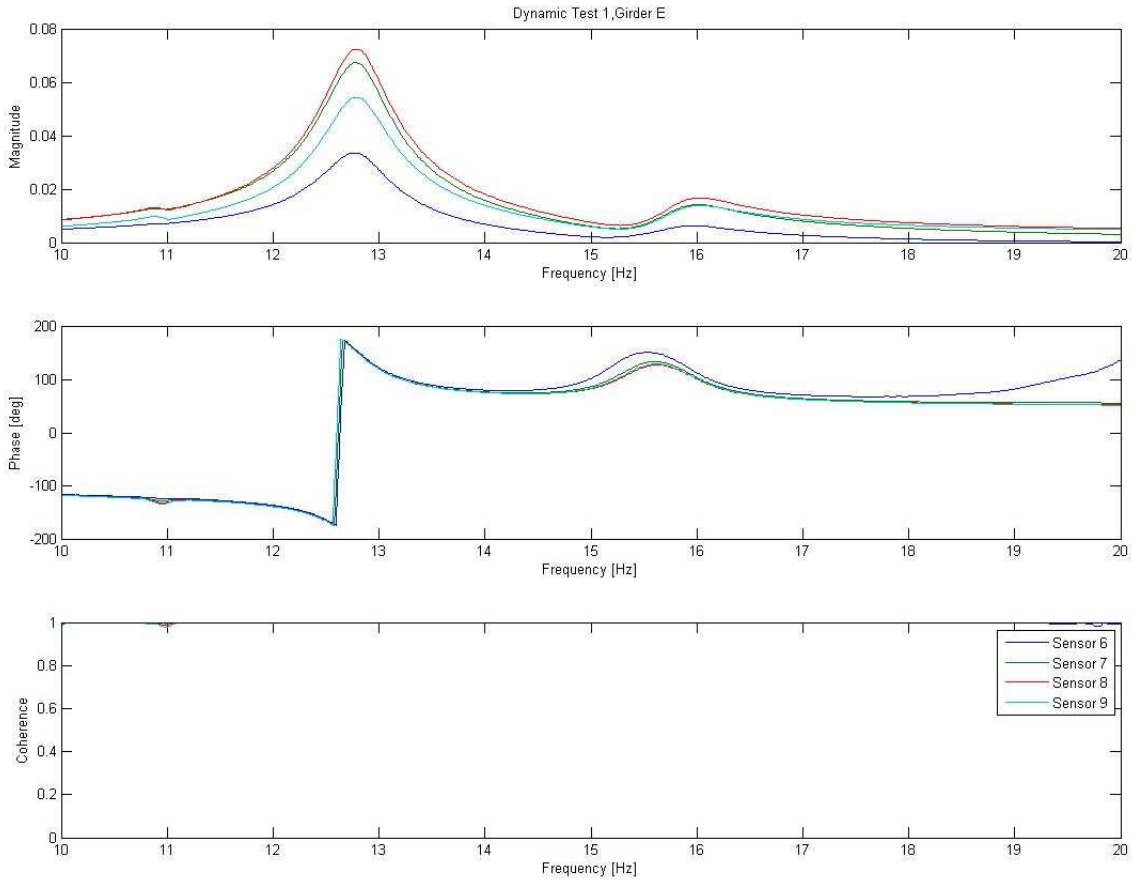

b)

Figure 30. Continued

In the range of 27 to 35 Hz, there were several apparent natural frequencies. For the scope of this research, one of these modes was chosen to monitor through failure. This mode occurred at a frequency of 29.39 Hz. This mode was chosen because examination of the phase plots show that sensors on like girders were tightly in phase and that sensors of unlike girders were tightly out of phase. This indicates another torsional

mode, which will further be designated as Mode 3. The approximate mode shapes are shown in Figure 31.

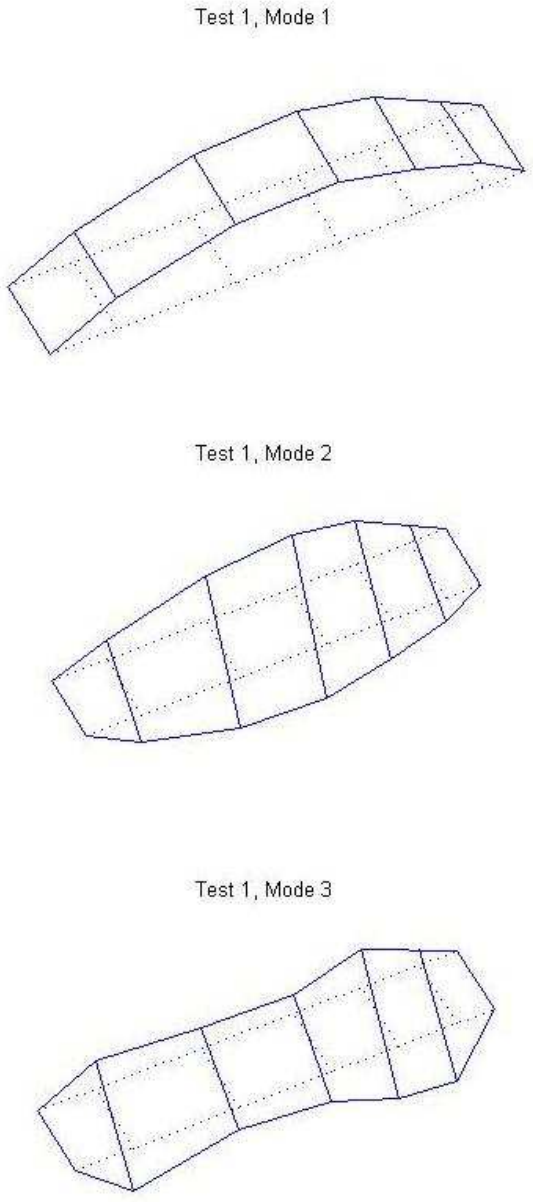

Figure 31. Mode shapes 1, 2, and 3 for Dynamic Test 1.

Fourteen subsequent dynamic tests were conducted according to the aforementioned testing schedule (Table 4). Mode 1, 2, and 3 were monitored for each test. The objective was to record any changes in mode shapes and/or natural frequencies throughout flexural yield and failure of the bridge. The results for each dynamic test are shown in Table 5.

Since this research is focused on the shifts in natural frequencies through yield and failure, it was convenient to report the percentage changes in each modal frequency on a test-by-test basis. These relative changes in modal frequencies are shown in Figure 32. Also for conciseness, a trend line is added which represents the change in average modal frequency for each test.

Table 5. Summary of natural frequencies

Natural Frequencies [Hz]				
Dynamic Test	Mode			
	1	2		3
		Lower Bound	Upper Bound	
1	12.79	15.64	16.01	29.39
2	12.82	15.60	15.98	29.42
3	12.76	15.51	15.89	29.42
4	12.77	15.48	15.88	29.44
5	12.72	15.40	15.81	29.37
6	12.70	15.33	15.75	29.36
7	12.72	15.42	15.77	29.38
8	12.93	15.62	15.95	29.49
9	12.98	15.58	15.95	29.49
10	13.10	15.94	16.22	29.56
11	13.20	16.11	16.36	29.50
12	13.26	16.26	16.47	29.40
13	13.16	16.07	16.33	29.24
14	13.24	15.73	16.03	28.68
15	12.58	N/A	14.64	27.92

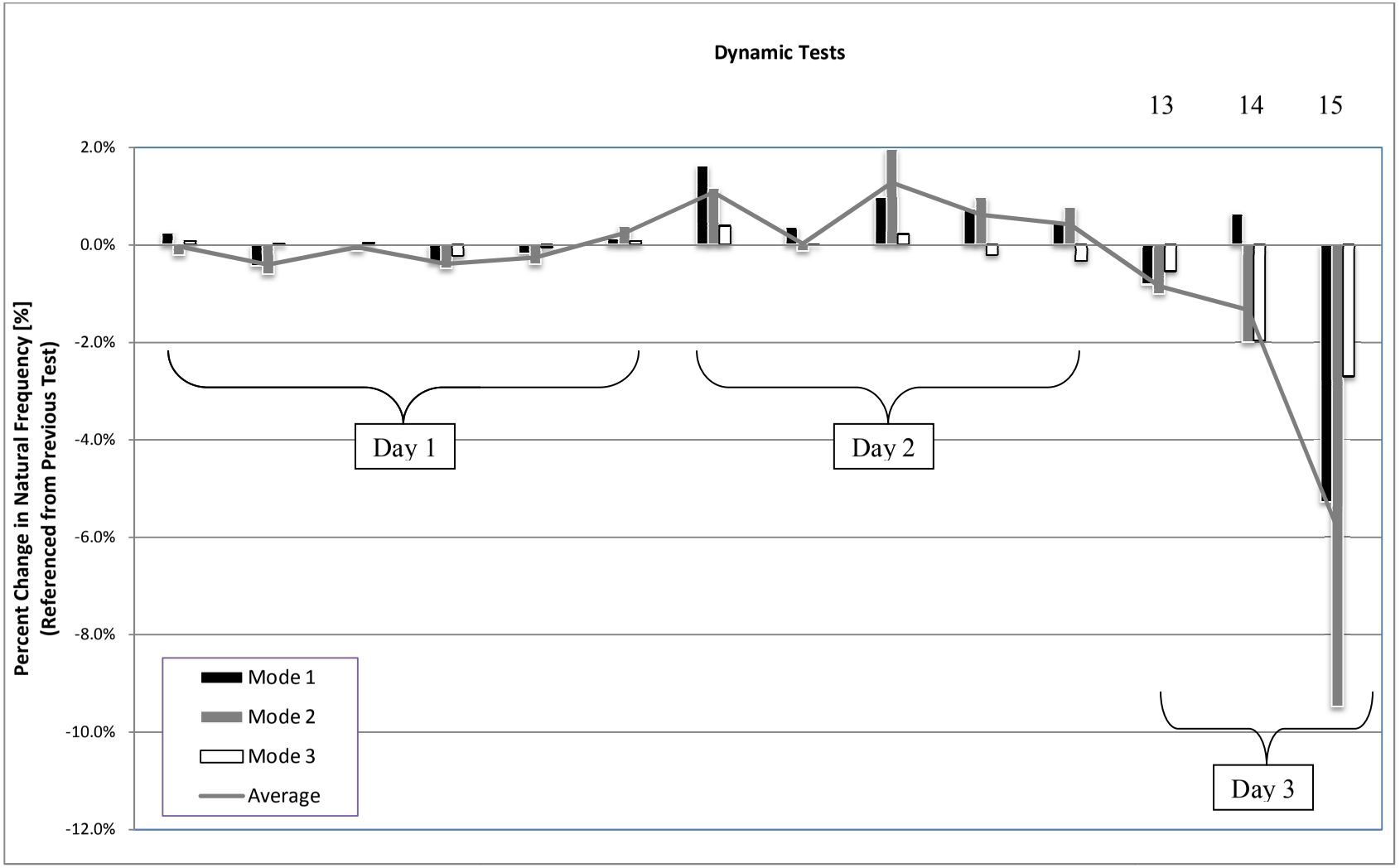

Figure 32: Relative natural frequency shifts throughout failure.

For the first seven dynamic tests, the dynamic response of the specimen remained fairly constant. A maximum average of -0.4% change in modal frequencies from test to test was recorded. This indicates little or no structural changes in the system. Also, the frequency shifts among these tests are all negative (i.e. the frequencies are decreasing). Essentially the bridge system is becoming more ductile. These tests were conducted sequentially on Day 1, and although exact temperatures were not recorded, it can be assumed that temperatures increased throughout the day. Previous research illustrates that warmer temperatures decrease dynamic stiffness structural systems, thereby reducing natural frequencies of (Zhao and DeWolf, 2002).

The first relatively large average modal frequency shift (+1.1%) occurs between Dynamic Tests 7 and 8. There are two possible reasons for this shift: 1) structural damage to the system or 2) temperature effects on the stiffness of the bridge. Prior to Dynamic Test 7 the researchers noted no girder damage and minimal deck damage (propagation of hairline cracks). Dynamic Test 7 was conducted on Day 1 at 3:57 p.m. and Dynamic Test 8 was conducted on Day 2 at 9:53 a.m. The exact temperatures were not recorded; however, the time difference implies that the temperature during Dynamic Test 8 was cooler than Dynamic Test 7. Reduced temperatures tend to increase structural stiffness and natural frequencies (Zhao and DeWolf, 2002), which is consistent with the observed frequency shift.

There was an average 0.0% change in modal frequencies between Dynamic Tests 8 and 9, indicating no structural changes in the system. There is an average +1.3% change in modal frequencies between Dynamic Tests 9 and 10, indicating an increase in

flexural stiffness. Once again, exact temperatures were not recorded for each test; however, it can be assumed that temperatures increased throughout the day which should have *decreased* the stiffness and natural frequencies. During the static point load test prior to Dynamic Test 10 one strain gage recorded over 8,000 με. This is the first recorded yielding of the system. It is important to note that the first yield of the system coincided with the largest increase in average natural frequencies.

Dynamic Tests 11 and 12 exhibited average increases in natural frequencies of 0.6% and 0.4%, respectively. According to temperature effects experienced on Day 1, a decrease in natural frequencies was expected from test to test, which is inconsistent with findings from Dynamic Tests 11 and 12. This indicates that the structural stiffness is increasing as the system becomes more yielded.

The static point load prior to Dynamic Test 12 was 1,330 kN (299^{k}). Therefore, the target load prior to Dynamic Test 13 was 1420 kN (320^{k}); however, the actual load sustained was 1310 kN (294^{k}). The load was removed at this point because of a crack that formed in the deck directly beneath the ram. The crack was primarily followed the top mat of reinforcement in the deck. The crack was approximately 400 mm (16 in.) long and 3.2 mm (0.13 in.) wide. Dynamic Test 13 was subsequently performed at 11:11 a.m. on Day 3. According to the temperature effects experienced between Days 1 and 2 the bridge specimen would exhibit higher natural frequencies; however, there was an average change in modal frequencies of -0.8%. This decrease in natural frequencies was attributed to the crack in the concrete deck which effectively reduced the specimen's flexural stiffness.

Prior to Dynamic Test 14, the concrete directly beneath the ram experienced somewhat of a localized bearing failure. There was a visible depression of the spherical bearing into the concrete. There was isolated spalling and delamination of the underside of the deck directly beneath the point load (Figure 33). Also the crack that previously formed propagated along the top mat of reinforcement in both directions to a final length of approximately 4.1 m (13 ft 5 in.). The crack expanded to approximately 13 mm (0.5 in.) wide (Figure 34). The average natural frequency change recorded in Dynamic Test 14 was -1.3%. This was the second largest decrease in average modal frequencies recorded throughout testing. The reduced stiffness was attributed to the aforementioned deck damage.

Figure 33. Delamination and Spalling Beneath Point Load at 1,420 kN (320^{k}).

a)

b)

Figure 34. Flexural cracks after a) 1,420 kN (320[k]) and b) failure, 1,490 (334[k]).

The bridge reached its ultimate capacity prior to Dynamic Test 15. At this point, the crack formed beneath the load point had opened to approximately 76 millimeters (3.0 inches) during the load test. After the load was removed the crack had a residual gap of approximately 38 millimeters (1.5 inches) as shown in Figure 34b. This crack was formed by de-bonding of the upper mat of reinforcement due to excessive compression. The majority of system damage was consolidated to the deck in the region surrounding the point load (i.e.: directly above Girder D). Damage consisted of large cracking, severe delamination on the underside of the deck, and spalling of the concrete. Dynamic Test 15 yielded a change in average natural frequencies of -5.8%. This was the largest decrease in modal frequencies recorded throughout testing. It is concluded that the severe damage of the deck above Girder D is the primary reason for the frequency shift.

Arguably more interesting than the modal frequency change is the FRF plot of Dynamic Test 15 (Figure 35). Specifically, the sensors oriented on Girder D do not show a local maximum for the lower bound frequency of Mode 2. However, there is an apparent resonance in the frequency range of 14-15 Hz. According to the changes in the upper bound frequencies for Mode 2, this is consistent with where the lower bound for Mode 2 would be predicted. It is likely that the resonance still exists in that range and is not being explicitly displayed in the FRF plot. This may be due to energy leakage from insufficient resolution of the frequency channels. Had the researchers been aware of this behavior an additional dynamic test would have been conducted with proper resolution; however, this was discovered after Bridge Specimen 1 had been disposed of.

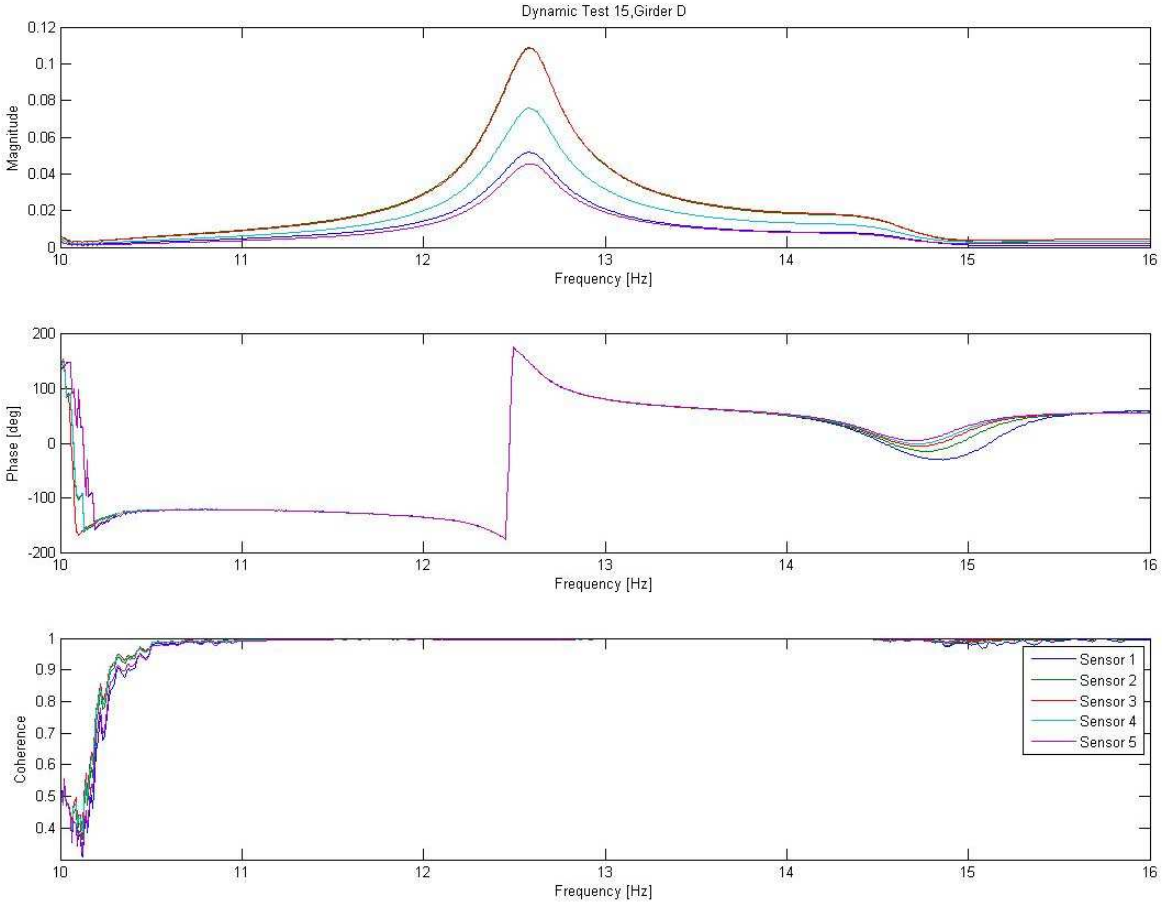

Figure 35. Dynamic Test 15, Girder D, 10-16 Hz.

While temperature is believed to have influenced the results of this test, it should be noted that there was very little change in mode shapes throughout testing, despite the severe deck damage the bridge had endured. There was an average change in natural frequencies between Dynamic Tests 1 and 15 of -5.4%.

CHAPTER IV

FINITE-ELEMENT MODELING

This chapter presents, in detail, the finite-element modeling of the 8th North Bridge specimens. The computer models were constructed and analyzed using the software, *ANSYS 12.1*. The models were calibrated to reproduce experimental results discussed in Chapter 3. To obtain a comprehensive representation of the bridge specimens and their multiple failure modes, four FEMs were constructed. Each model contained various elements to accurately depict experimental behavior.

Chapter 4 is divided into four sections. First, the element and material properties used in FEA will be discussed. The next three sections present the flexural model, beam shear model, and punching shear models, respectively.

Element and Material Properties

The mathematical representation of physical elements in *ANSYS* is prescribed by four criteria: element type, real constants, material association, and key options (KEYOPTs). The element type designates the element shape, DOFs, and modeling capabilities. Real constants are a set of values which correspond to the element type. Material association provides the constitutive relationships. Key options activate and specify special features of the elements.

The primary elements used in this research are SHELL181 and SOLID65. In all cases the girder webs and flanges were modeled with shell elements and the concrete deck was modeled with solid elements. Three connecting elements were used in this

research: TARGE170, CONTA173, and LINK8. The contact and target elements were used to model the bond at the concrete/steel and concrete/grout interfaces. The link element was used to model the welded stud connection between the precast deck panels. Each element will be further described in detail.

The SHELL181 element is a quadrilateral planar element with six DOFs at each node (three translational and three rotational). The element has 12 real constants. The first real constant was the only specified value which describes a uniform thickness of the element. *ANSYS Workbench* defaults to a full integration scheme (KEYOPT(3) = 2) and *ANSYS Classic* defaults to a reduced integration scheme with hourglass control (KEYOPT(3) = 0). All other default settings were used.

The SOLID65 element is an eight-node solid element with three translational DOFs at each node. Special features of this element include rebar reinforcement and support of a brittle concrete material model, which is capable of compression crushing and tension cracking. Real constants for SOLID65 specify the reinforcement properties by designating a reinforcement material, volumetric ratio of reinforcement to base material, and two angles which describe the orientation of reinforcement. The first angle (θ) describes the orientation measure from the local x to y axes, and the second angle (φ) is the angle measured from the local x-y plane towards the z axis. Up to three reinforcements can be used.

The concrete material model predicts crushing and cracking. The crushing feature is based on the compressive strength of the concrete (f'c) and the cracking feature is based on an ultimate tensile stress (f_r), which was calculated according to:

$$f_r = 0.7\sqrt{f'c} \qquad (SI\ Units)$$

$$f_r = 7.5\sqrt{f'c} \qquad (English\ Units)$$

At each iteration step in the solution routine the software calculates the principal stresses at all Gauss integration points. If the stresses exceed the maximum tensile/compressive stress, the element is considered to be cracked/crushed at that integration point along a plane normal to that of the exceeded principal stress. The element stiffness at that integration point in the damaged direction is then set to zero, which effectively reduces the overall element stiffness. When an element is completely cracked/crushed the resulting forces are transferred to adjacent undamaged elements. Forces are transmitted across a crack according to shear transfer coefficients. For open cracks, a shear transfer coefficient (β_t) of 0.2 was used, meaning that 20% of the shear was transferred across the crack. For closed cracks a shear transfer coefficient (β_c) of 0.6 was used. These values were selected based on previous research (Julander, 2009).

When a crack initiates the nearby stresses instantly drop to zero which often causes convergence issues. A stress relaxation option is offered to avoid this, which gradually reduces stresses surrounding cracks to zero. Stress relaxation was activated by setting KEYOP(7) to 1. All other default settings were used.

Deformable bodies in *ANSYS* are joined together by contact regions. A contact region is defined by a pair of elements, namely contact and target elements. Contact elements overlay elements of a body (the contact body) and target elements overlay the elements of a separate, unconnected body (the target body). As the contact body moves

towards the target body, the contacting elements prevent penetration (i.e. overlap) or separation of the body elements by supplying a reactionary force to both bodies. The contacting elements take the same shape as their underlying elements and have the same DOF's.

The behavior of contact and target pairs is described solely by the input of the contact element. For CONTA173, the initial behavior was set to bonded by setting KEYOPT(12) to 5. A pure penalty algorithm was used for the contact formulation by setting KEYOPT(2) to 1. This formulation models the contact as a set of normal and tangential springs. This stiffness of the contact can be updated each iteration step by setting KEYOPT(10) to 2. In *ANSYS Workbench*, the default contact element is CONTA174, which is simply a higher order version of CONTA173 and is used to overlay elements with mid-side nodes. Since no elements with mid-side nodes were used, CONTA174 elements behaved identical to CONTA173 elements.

Each pair of contacting elements shares an exclusive real constant set. The real constant set for the TARGE170 and CONTA173 elements contain 26 values. The 3rd and 12th real constants designate the normal and tangential stiffness factors (FKN and FKT), respectively. In some cases, a pinball radius was used by specifying the sixth real constant. The pinball region is defined as a spherical boundary radiating from nodes on the target surface. Nodes on the contacting surface within this region have a closed status, meaning that the contact is in effect. Contact elements that are outside of the pinball radius have an open status, and no forces are transmitted across the contact region.

The LINK8 element is a simple spar element. It has two nodes with three translational DOF's at each node. Two real constants are associated with the LINK8 element: cross sectional area and initial strain. The LINK8 element has no KEYOPTs.

Concrete and steel properties were determined experimentally. Five concrete cylinders were cored out of the deck. The cylinders were 203.2 mm (8 in.) tall and 101.6 mm (4 in.) in diameter. The cylinders were crushed in uni-axial compression tests, and the compressive force was measured during each test. The five cylinders had an average compressive stress of 57,000 kPa (8,300 psi). The corresponding tensile strength of the concrete was calculated as 4,700 kPa (680 psi). The elastic modulus of concrete was calculated as:

$$E_c = 3.32\sqrt{f'c} + 6{,}895 \qquad (SI\ Units)$$

$$E_c = 40{,}000\sqrt{f'c} + 1{,}000{,}000 \qquad (English\ Units)$$

which resulted in a value of 32,000 MPa (4,640 ksi). The value of Poisson's ratio was assumed to be 0.18.

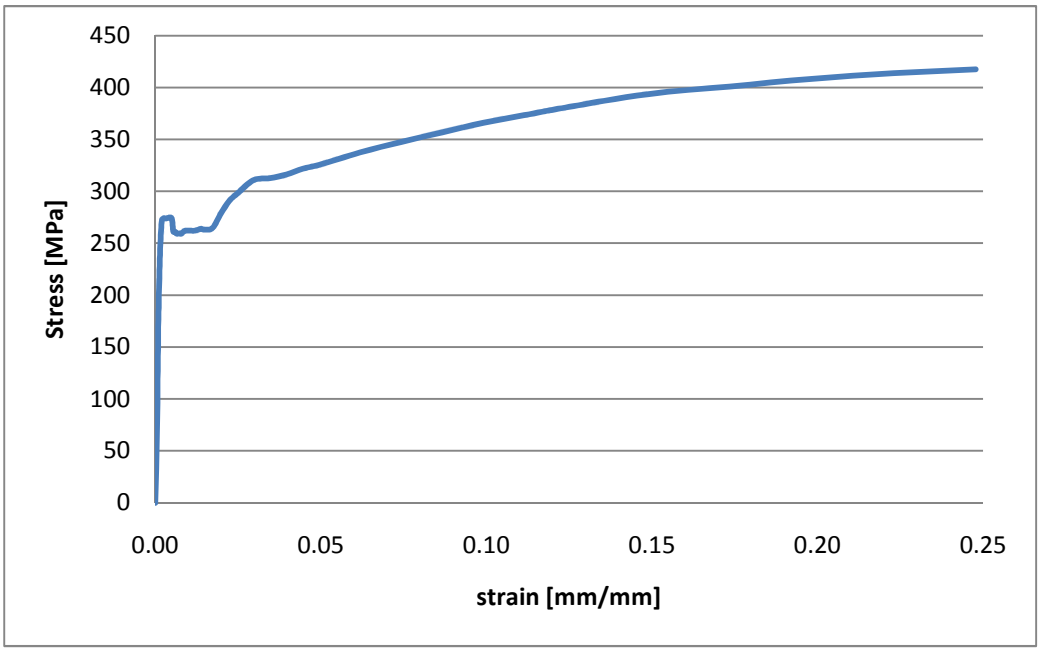

Figure 36. Experimental stress-strain curve for steel.

Two steel coupons were excised from the web of Girder B. These coupons measured approximately 762 mm (30 in.) long, 25.4 mm (1 in.) wide, and 9.5 mm (0.375 in.) thick. Tensile tests were performed on the coupons. Loads were measured with corresponding deformations. Loads were divided by the cross sectional area to obtain stresses. Deformations were divided by the original specimen length to obtain strains. A resulting stress-strain curve was built for each test (Figure 36). The yield stress of the steel (f_y) was determined to be 260 MPa (38 ksi). The steel had an ultimate stress (f_u) of 410 MPa (60 ksi) at a strain of 0.25. It was assumed that the elastic modulus (E_s) and Poisson's ratio (v) were 200,000 MPa (29,000 ksi) and 0.3, respectively.

Flexural Model

Model construction and analysis

A comprehensive two-girder FEM was constructed to replicate the flexural behavior of Bridge Specimen 2. The model was constructed using *ANSYS Workbench*, which creates standalone analysis systems in the project schematic. A static structural analysis was implemented.

The first component in the standalone analysis is the Engineering Data. A nonlinear steel material was defined with a multi-linear isotropic hardening plasticity model using experimental results. The primary mode of failure witnessed in the laboratory was a splitting failure of the concrete at the top layer of reinforcement. It was not practical to model this type of localized failure on a full-scale bridge specimen model. Therefore, the observed failure in the laboratory was not replicated directly. To obtain a different yet equivalent failure of concrete in the FEM, a bilinear stress-strain curve was implemented for concrete. It was analyzed in Chapter 3 that the splitting failure initiated when the concrete stress reached a value of 19.7 MPa (2,850 psi). Therefore, the yield stress was taken to be 19.7 MPa (2,850 psi) and the tangent modulus was taken to be zero. The elastic-plastic material model for concrete has been successfully utilized to replicate concrete failures in previous studies (Barbosa and Ribeiro, 1998).

The next component in the analysis is the Design Modeler application, which is a solid-modeling computer-aided drafting (CAD) program. The Design Modeler was used to create the geometry of the FEM. The girders were created completely out of surface bodies, which are two dimensional objects in a three dimensional design space. Surface

bodies are meshed into planar elements. Appropriate thicknesses were assigned to different components of the girder (i.e. web, flanges, and stiffeners). The individual surfaces were joined together with the Joint function. This was necessary to ensure the bodies were connected by sharing consistent nodes in the meshing process. As a design simplification, the deck was modeled as a monolithic feature rather than separate panels. A three-dimensional solid body was created using the Extrude function to represent the deck. Solid bodies are meshed into solid elements. Super-elevation was not accounted for in the model. The grouted haunch was also excluded in the model, and therefore the bottom of the deck coincided with the top of the girder flange.

The Mechanical application is where the finite-element modeling, analysis set up, and solution takes place. First, the geometry is automatically imported from the Design Modeler file. Appropriate materials were assigned to the girders and deck. Next, contact regions were set up to connect the deck to the girders. The contact and target surfaces were automatically scoped to the top flange and deck underside, respectively. The normal stiffness factor (FKN) value ranges from 0.01 to 1.0. Lower FKN values help convergence in applications where large bending occurs (ANSYS, 2005b). A value of 0.01 was used here. By default, the program checks the contact status for both the contacting and targeting elements, also known as symmetric behavior. To save computational time the behavior was set to asymmetric, meaning that the program only checks one of the elements in the pair.

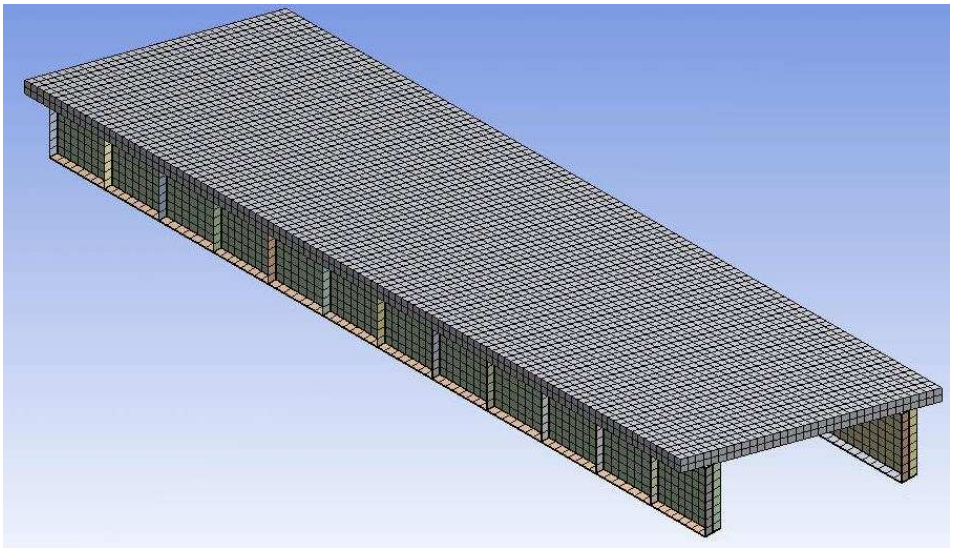

Figure 37. Flexural FEM mesh.

The final step in the modeling portion is the mesh. To save computational space, the majority of the web stiffeners on the unloaded girder were suppressed, meaning they would not be included in analysis. All bodies were assigned a quadrilateral face mapping. All mid-side nodes were dropped. The model was then meshed (Figure 37). By default, *Workbench* meshes all surface elements into SHELL181 elements and all solid elements into SOLID185 elements. Contact regions are meshed into TARGE170 and CONTA174 elements.

The Mechanical application was also used to set up the static structural analysis. The force convergence was activated with the default settings (0.5% tolerance about a program calculated value). One load step was defined. An overall analysis time of 1 second was used. This is not physical time, but rather an arbitrary parameter within *ANSYS* which defines load steps. A value of 1 second was used to conveniently relate output results as a percentage of the applied load. An initial 50 sub-steps were defined,

meaning that the program will divide the load into 50 increments and apply them individually. The large deformation effect was activated which means, at each sub-step, a new stiffness matrix is calculated based on the deformed geometry. By default, *ANSYS* uses the Newton-Raphson approach to solve nonlinear analyses.

Boundary conditions were then applied. A remote force was scoped to the top surface of the deck and placed at a location of 0.4*L* and directly above the girder representing Girder C. The pinball radius of the force was set to 102 mm (4.0 in) which was equal to the radius of the spherical bearing. When the pinball radius is specified, the program sets up a link among all elements on the scoped body that fall within the pinball region. The link is a pair of TARGE170 and CONTA174 elements with a multi-point constraint (MPC) formulation instead of a pure penalty formulation. The load is then applied to one node within the region (the pilot node). The MPC formulation effectively distributes the force among nodes that fall within the pinball radius (Figure 38). Constraints created this way reduce undesired stress concentrations at the location of the applied load.

At the reactions on one end of the bridge (support line 1), the vertices where the web, web support stiffener, and bottom flange coincided were assigned a zero displacement in all three directions (pin support). On the opposite end of the bridge (support line 2), the analogous vertices were assigned a zero displacement in the vertical and transverse directions. The longitudinal directions were free to deform to represent the rollers used in the laboratory (roller support). These support conditions result in highly inaccurate stress concentrations near the support.

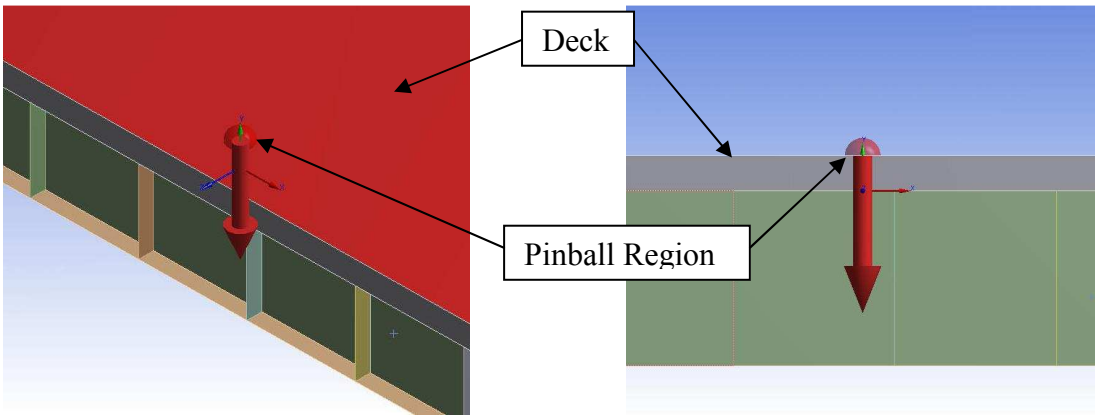

a) b)

Figure 38. Remote force pinball constraint: a) isomeric view and b) transverse view.

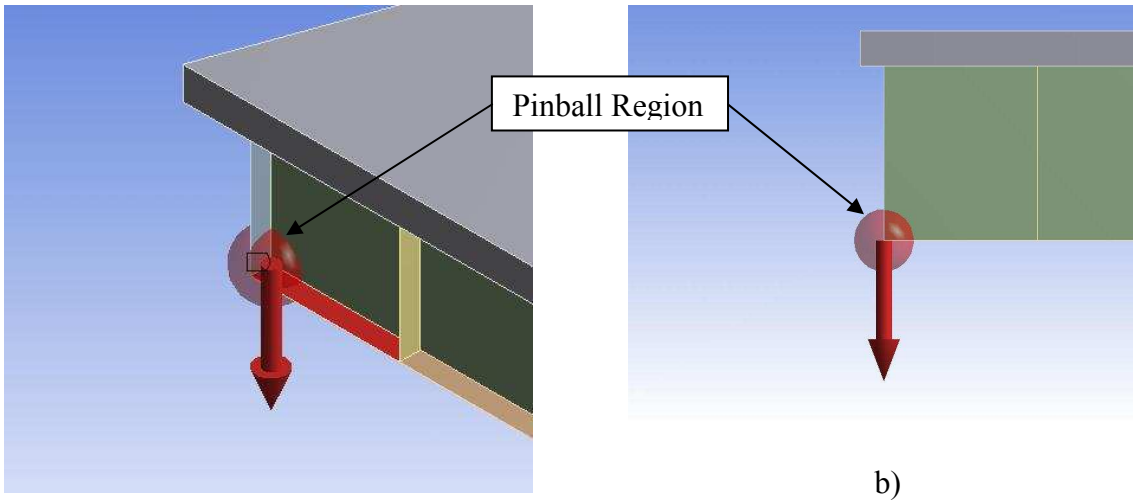

b)

a)

Figure 39. Girder support pinball constraint: a) isomeric view and b) transverse view.

To mitigate this effect a rigid surface constraint was implemented in the same manner as the applied load. This was done by constructing a remote force at the supported vertices. The force was scoped to the bottom flange. The pinball region was specified as slightly greater than the width of the flange (Figure 39). The force assigned to the supported vertices was non-zero and negligible compared to the ultimate load applied. Effectively, this set up a constraint equation among elements in the pinball radius and the pilot nodes (supported vertices).

ANSYS Workbench is relatively limited in its analysis capabilities when compared to *ANSYS Classic*. This is because all of the features of *Classic* have yet to be fully implemented to the graphical user interface in *Workbench*. To access these features, a command script was set up in the static structural branch. The *Classic* preprocessor was accessed with the /PREP7 command. Since *Workbench* defaults to a full integration scheme for SHELL181 elements, reduced integration scheme with hourglass control was activated by setting KEYOPT(3) = 0 in the command script for all steel bodies. This was done to save computational time and to help convergence. The SOLID 186 elements were changed to SOLID65 elements. The tangential stiffness factor (FKT) for CONTA174 elements representing the girder-deck connections were modified to 0.5. This means that 50% of the shear flow would be transmitted between the girder and deck. This was done to represent the somewhat complete composite action measured in the laboratory.

The constraint equations set up at the girder supports are by default a force-distribution constraint. However, a rigid surface constraint was desired. A nodal

detection of contacting points within the pinball radius was specified by setting KEYOPT(4) = 2 for CONTA174 elements at the supports. Also, by default, the contact pairs include all DOFs. However, the support conditions in the laboratory allowed for rotation about the transverse axis. The transverse rotations were permitted by setting KEYOPT(4) = 011111 for TARGE170 elements at the supports. The preprocessor was exited using the /SOLU command. The SOLVE command was then issued to initiate the analysis routine (ANSYS, 2005a).

While the incremental loading method is sufficient to predict elastic and post-elastic behavior, it does not accurately predict ultimate capacity. In order to compute the ultimate flexural capacity of the system, a second analysis was implemented with the aforementioned modeling components. The only difference was that the automatic time stepping function was activated, in which program automatically predicted a proper load increment to apply to the model. If the model failed to converge after a number of iterations, the load increment was bisected and the load was reapplied. The applied load became smaller and smaller with each bisection. Eventually, the model failed to converge at a tolerable load increment, which was considered the ultimate capacity.

Results and comparison

It was concluded that the highest quality data was gathered during Flexural Test C because of the revised support reactions and string-pot assemblies. Therefore, this data was the focus of calibrating the analytical model.

The FEM distributed the load to the reactions. These reactions were recorded and compared against experimental findings (Figure 40). It can be seen that the both the

experimental and analytical model distribute the load in a similar manner. While the percent distribution varies slightly in the experimental model for all reactions, the percent distribution remains fairly constant in the FEM for all reactions up until approximately 1,200 kN (270^{k}). At this point, the percent distribution begins to deviate, which agrees with experimental findings. This load level is the approximate yield load of the system.

The FEM predicts that relatively little load is transferred to the unloaded girder, which agrees with experimental results. A maximum of -3.2% of the applied load (uplift) was transferred to the off-girder in the FEM. This compares well to -1.6% of the applied load transferred to the off-girder in the experimental model.

It is shown that the larger deviations in percent load distributed occur at low load levels. At a load of 31 kN (7.0^{k}) the FEM overestimates Reaction C1 by 5.86% of the applied load. This is the maximum deviation among all reactions prior to yielding. After yielding, the models still show agreement. In this region, the FEM overestimates Reaction C2 by a maximum of 6.41%. This is the maximum deviation among all reactions after yielding.

Furthermore, Reaction C1 carries the maximum load for both models. At an applied load of 1,490 kN (336^{k}), which is within 4% of the ultimate experimental load, there is only a 1.34% difference in percent distribution at Reaction C1 for both models. This would be the controlling shear reaction in design. Essentially, this shows that the FEM behaves very well in the post-elastic range for load distribution, which was the objective of the model.

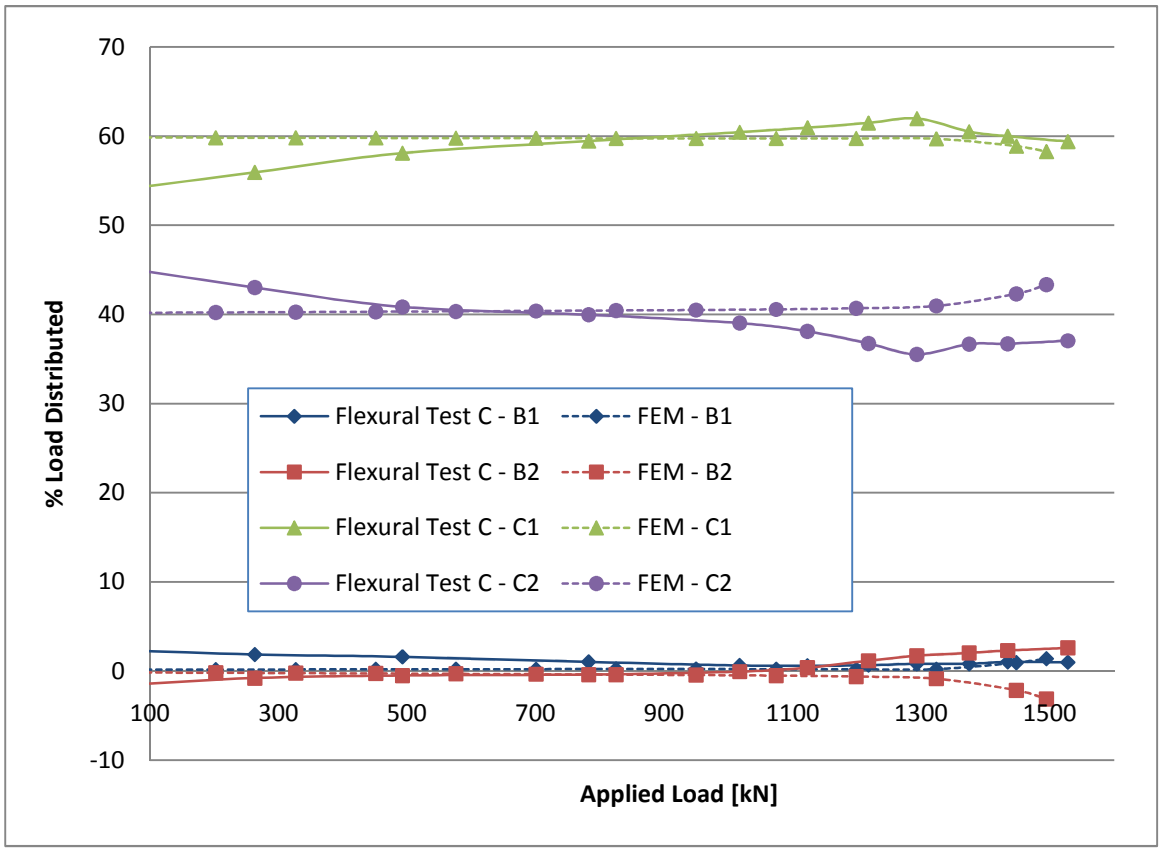

Figure 40. Flexural Test C load distribution comparison.

The deflections of Girder C at 0.5*L* were recorded at each sub-step in the FEM. These deflections are plotted with the experimentally measured deflections at the same location (Figure 41). Overall, the analytical results show great agreement to the experimental results. The deflection curve is quite sensitive to the FKT factor used for the contacting regions between the girder and deck. This was expected because the factor directly relates to the degree of composite action between the two. In the elastic portion, both curves exhibit a near identical stiffness. This is a good indicator that the appropriate level of composite action was obtained in the FEM.

In the plastic region, there is a slight deviation between the two models. The experimental model has a relatively straight plastic path and the FEM has a slightly curved path. Nonetheless, the two paths correlate extremely well.

The post-elastic behavior verifies that elastic-plastic failure criterion for concrete was appropriate for this application. The failure replicated in the FEM was not the same as that observed in the laboratory. However, an equivalent plastic failure was obtained in the FEM.

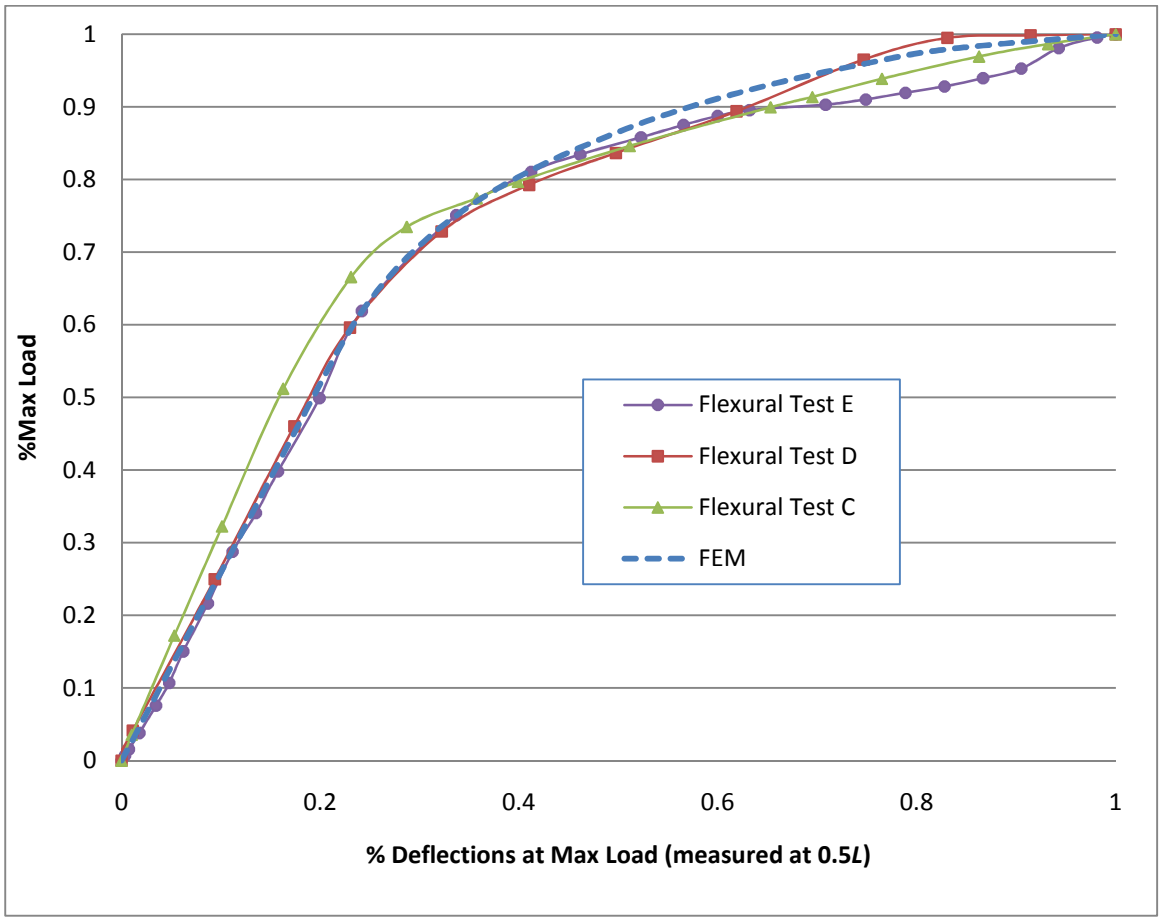

Figure 41. Flexural deflections comparison.

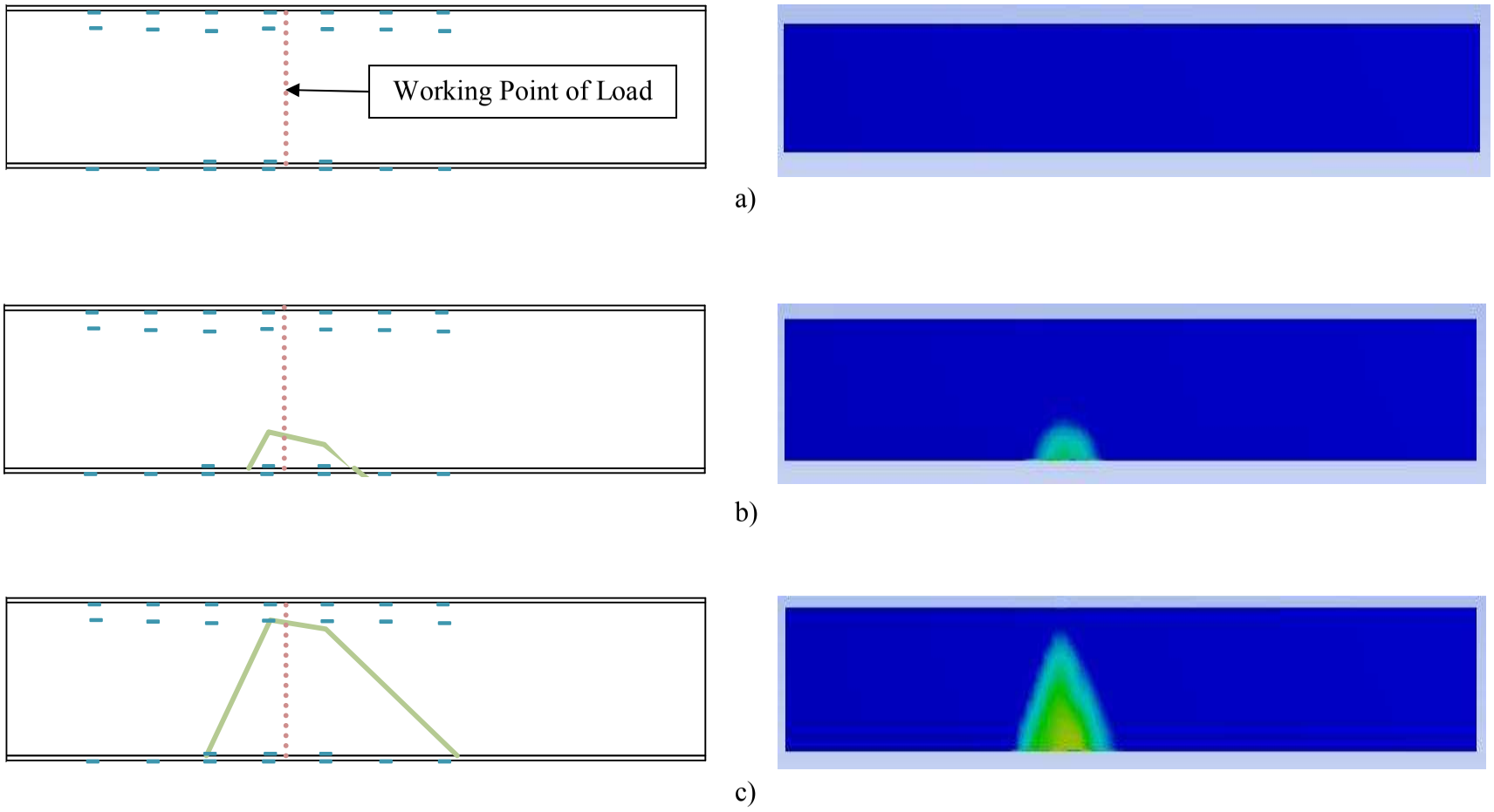

Figure 42. Plasticity region for Flexural Test C comparison at a) 493 kN (111k), b) 783kN (176k), and c) 1,370 kN (309k) (experimental on left, FEM on right).

One of the solution results in *Workbench* is the Equivalent Elastic Strain. This strain is also known as the Von Mises strain. It is directly related to the principal stress of the element. The Equivalent Elastic Strain must be calculated in order to compute the Equivalent Plastic Strain. The Equivalent Plastic Strain is simply the difference between the Equivalent Elastic Strain and the proportional limit. In the case of a multi-linear stress-strain curve as used for the steel girders, the proportional limit is simply the yield strain. *Workbench* conveniently creates a contour plot of the plastic strain. Figure 42 shows that the computer-predicted plasticity region maps fairly well to the experimentally measured plasticity region at various load levels. At larger loads, the FEM predicts a smaller plasticity region than the experimental model. At these loads, the FEM accurately predicts the cross-sectional depth which has yielded directly beneath the applied load; however, the longitudinal distance of plasticity predicted by the FEM is smaller than experimental results.

The FEM was analyzed a second time with the automatic time stepping function activated. The FEM failed to converge at an applied load of 1,500 kN (338^{k}). Investigation of the stresses at this load indicated the majority of the cross section at the applied load had entered plasticity. Deflections rose dramatically. For these reasons, this was considered the ultimate load. When compared to the maximum experimental load of 1,560 kN (350^{k}), the FEM underestimated the ultimate load capacity by 3.4%. This is another good indicator that the specimen was properly modeled.

At the FEM's ultimate load, -1.77% of the load was transferred to the unloaded girder (uplift). Since this value is relatively small, an approximation of the moment

carried by the cross section can be calculated by idealizing the bridge as a two-dimensional beam problem. The reactionary forces of the loaded girder were multiplied by their distance from the applied load to obtain a moment. At the maximum sustained load in the FEM, two moment values were calculated and averaged to a value of 4,020 kN-m (2,960 k-ft). When compared to Flexural Tests E and C, the ultimate moment approximated by the FEM differed by -2.9% and 2.5%, respectively.

Beam Shear Model

Model construction and analysis

A comprehensive two-girder FEM was constructed to replicate the beam shear behavior of Bridge Specimen 2. The model was constructed using *ANSYS Workbench*. The software provides a linear buckling analysis standalone system, which evaluates eigenvalues and eigenvectors. Preliminary models using this analysis system yielded poor results. Therefore, in order to predict the buckling failure witnessed in the laboratory, a nonlinear buckling analysis was conducted. A nonlinear buckling analysis is very similar to a static structural analysis. The engineering data, geometry, and finite-element modeling were defined in a similar manner as the flexural model.

First, materials were defined in the Engineering Data component system. A nonlinear steel material was defined with a multi-linear isotropic hardening model based on experimental results. An elastic concrete material was defined using experimental results; no nonlinearities were defined. This was justified because the experimental

deflections for the beam shear tests remained nearly elastic through the ultimate capacity (Figure 22).

The geometry of the FEM was created in the Design Modeler application. The geometry was identical to that of the flexural model, except for one key point. The web stiffener nearest the loaded reaction was left unconnected to the bottom flange, as observed in the laboratory. The geometry was imported into the Mechanical applications. Appropriate materials were assigned to the girders and deck panels. Next, contact regions were set up to connect the deck to the girders. The contact and target surfaces were automatically scoped to the top flange and deck underside, respectively. The FKN value was set to 0.01. The contact status check was set to asymmetric.

The next step was the mesh. To save computational space, all of the intermediate web stiffeners on the unloaded girder were suppressed, meaning they would be not included in analysis. All bodies were assigned a quadrilateral face mapping. It was specified to exclude all mid-side nodes in all elements created. Because the focus of interest in the beam shear model was very near the reaction, a refinement option was created, which controls the element size at a certain location. Refinement controls are assigned to bodies and are given a value of 1, 2, or 3. A refinement control of 1 provides minimal refinement and a value of 3 provides maximum refinement. On the loaded reaction, all bodies of the girder falling within $0.83L$ and $1.0L$ were assigned a refinement control of 1. The model was then meshed (Figure 43).

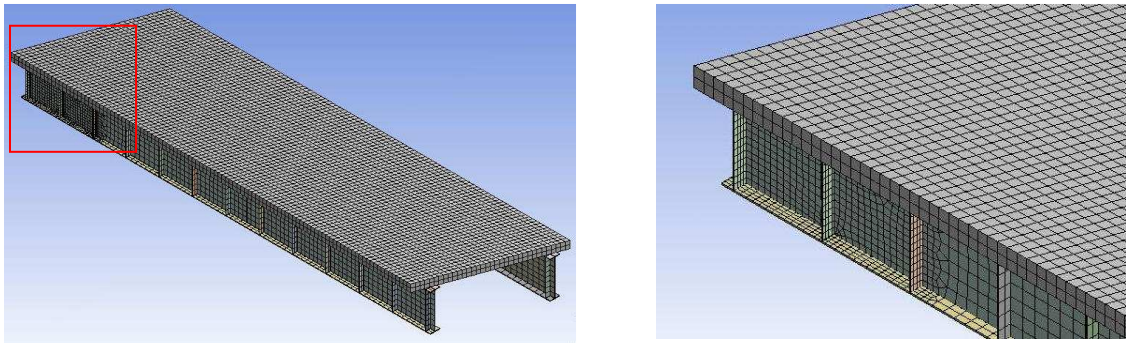

a) b)

Figure 43. Beam shear mesh: a) overall and b) local refinement control.

The static structural analysis was then configured. The force convergence was activated with the default settings (0.5% tolerance about a program calculated value). One load step was defined in which an overall analysis time of 1 second was used. The automatic time stepping function was set to program controlled. Using this setting, the software predicts the appropriate load increment and attempts to converge to a solution. When a solution is not converged after a number of equilibrium iterations, the load step is bisected and reapplied. Eventually, the solution will fail to converge, which is considered buckling. The large deformation effect was activated to obtain a more accurate solution.

Boundary conditions were then applied. A remote force was scoped to the top of the deck directly above the girder representing Girder B. The force was located at a longitudinal location of 0.88L. A pinball region was created with a radius of 102mm (4.0 in.) as shown in Figure 38.

Supports were created in the same manner as the flexural model: assigning zero displacements in all directions to the four vertices created by the bottom flanges, webs,

and web support stiffeners. At one end of the bridge, the supports were allowed to translate in the longitudinal direction. To reduce stress concentrations at the supports, surface constraints were then constructed in the same manner as the flexural model.

A command script was inserted into the static structural environment branch. The *Classic* preprocessor was accessed with the /PREP7 command. Since *Workbench* defaults to a full integration scheme for SHELL181 elements, reduced integration scheme with hourglass control was activated by setting KEYOPT(3) = 0 in the command script for all steel bodies. This was done to save computational time and to help convergence. The SOLID186 elements were changed to SOLID65 elements. The tangential stiffness factor (FKT) for CONTA174 elements representing the girder-deck connections were modified to 0.5. For CONTA174 elements at the supports, a nodal detection of contacting points within the pinball radius was specified by setting KEYOPT(4) = 2. The transverse rotations at the support constraints were permitted by setting KEYOPT(4) = 011111 for TARGE170 elements. The preprocessor was exited using the /SOLU command. The full Newton-Raphson analysis procedure with adaptive descent turned off was specified with the NROPT command. This setting is typical of nonlinear buckling analyses. The analysis routine was initiated with the SOLVE command.

Results and comparison

Given the structural damage to the bridge system prior to Beam Shear Test C, it was concluded that Beam Shear Test B would replicate more accurately the conditions in the field. Therefore, Beam Shear Test B was the target for calibrating the FEM. A static load greater than that recorded in the laboratory was applied to the model. The automatic

sub-step predictor broke the load into increments and solved the model for each load increment. When the solution failed to converge, the load increment was bisected and reapplied. Eventually, the program was unable to converge to a solution.

In order to verify that the unconverged solution was in fact caused by buckling, the results needed to be inspected. In a nonlinear buckling analysis, the mode shape is not explicitly predicted, although stress and strain plots can be examined in order to extrapolate the deflected shape.

a)

Figure 44. Beam shear buckling comparison: a) experimental buckled shape and b) FEM principal stresses.

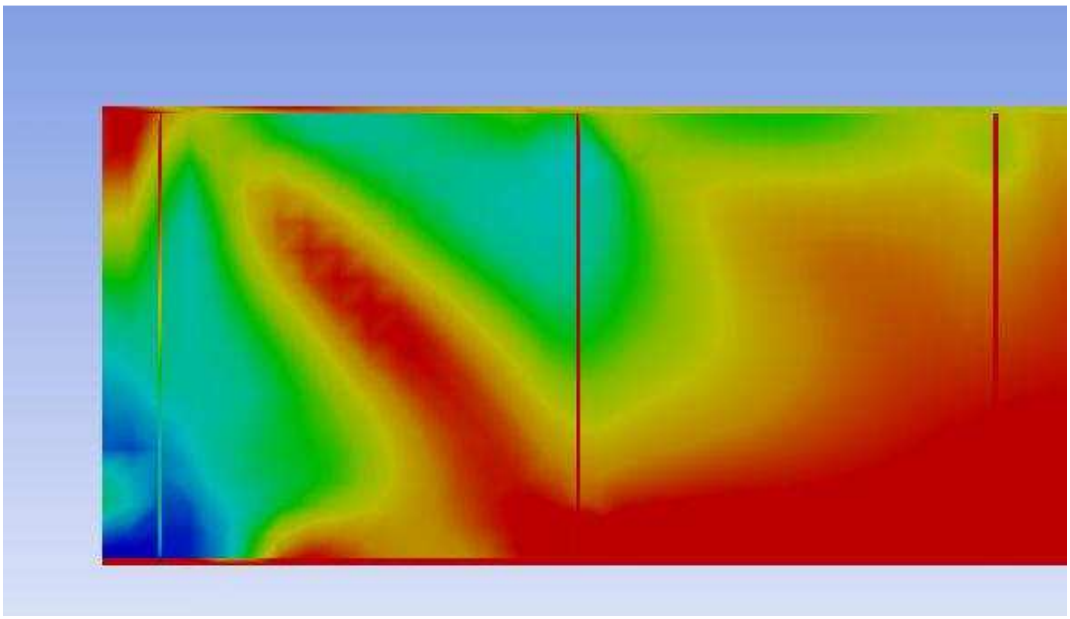

b)

Figure 44. Continued

Figure 44 shows the FEM principal stresses at the last converged solution in the analysis. The plot clearly shows that a tension-strut is forming in the same area, shape, and direction as the experimentally buckled shape. This suggests that the subsequent un-converged solution in the FEM is indeed a post-buckling tension-strut failure.

The last converged solution in the FEM correlated to an applied load of 1,600 kN (360^{k}). This load is 5.3% greater than the experimentally measured applied load at buckling failure, which was 1,520 kN (341^{k}). More importantly, the last converged solution in the FEM correlated to a maximum shear reaction of 1,400 kN (315^{k}). This shear force is 4.6% greater than the experimentally measured shear force at buckling

failure. For these reasons, it was concluded that the primary mode of buckling failure was properly obtained in the FEM.

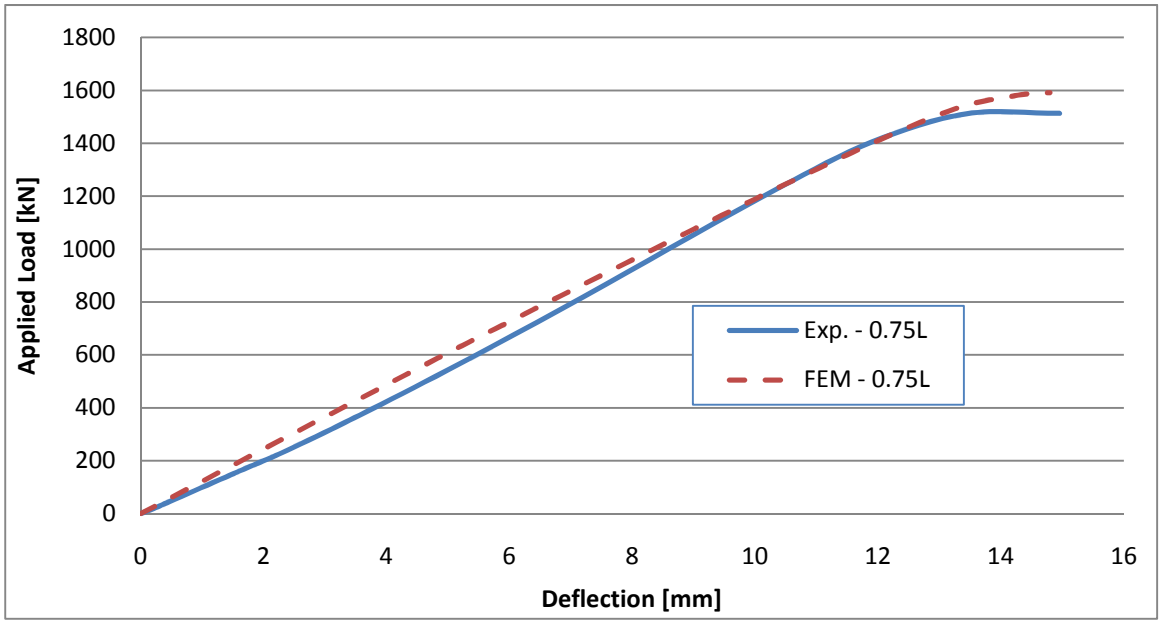

Figure 45. Beam shear deflections comparison.

While the ultimate buckling load is important to bridge design, it was necessary to verify the FEM elastic behavior in shear loading. This was done by comparing the deflections measured at the nearest quarter-span location for the experimental and analytical models (Figure 45). The load-deflection curves show very good agreement between the models. The FEM path is a constant slope until approximately 90% of the maximum sustained load. The experimental model exhibits a slightly lower stiffness initially than the FEM; however, the experimental path converges with the FEM path at an applied load of approximately 1,200 kN (270^{k}). For both models, the near-buckling

deflections are similar, although the FEM predicts slightly higher loads near failure. Overall, the FEM deflections exhibit high correlation to experimental deflections.

Punching Shear Models

Model construction and analysis

Two punching shear FEMs were created and analyzed in *ANSYS Classic*. One model consisted of a single continuous panel, and the other consisted of two independent panels connected together by a transverse joint. The models were constructed in Ansys Parametric Design Language (APDL) format. The continuous panel model will be discussed first.

The continuous panel model is relatively simple. It consists of a square slab of solid elements supported along two opposing edges (Figure 46). The boundary conditions of the slab were critical. It was concluded that transverse rotations of the panels were somewhat fixed above the girder. To mimic this, steel bearings were created beneath the concrete slab along opposing edges. These bearings were given a thickness of 15.9 mm (0.625 in.).

First, concrete and steel material properties were defined. Bilinear isotropic hardening data was input for the steel using experimental results. Cracking data was input for concrete consisting of a tensile stress and the two shear transfer coefficients. The crushing feature was turned off due to convergence issues

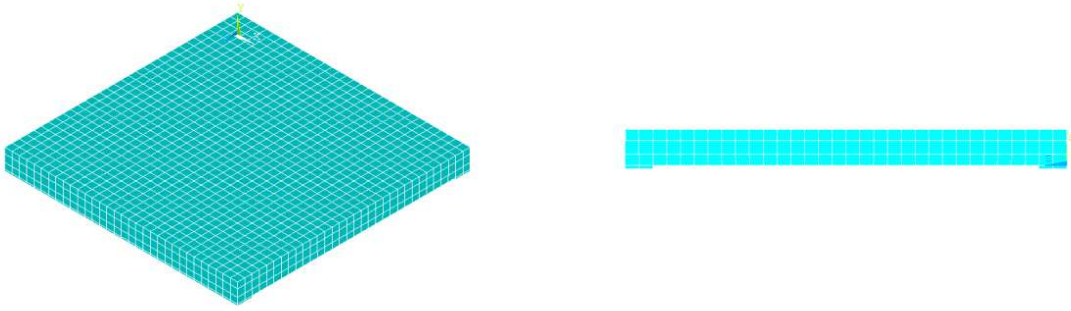

a) b)

Figure 46. Continuous panel model mesh: a) isometric view and b) profile view.

A SOLID65 element was defined for the concrete. After initial analysis it was determined that the model yielded better results if the reinforcement was modeled as separate elements rather than smearing the reinforcement throughout the solid elements. Therefore, a SHELL181 element was defined. Rotational DOFs were neglected by setting KEYOPT(1) to 1, effectively turning them into membrane elements. This way, moments could be transmitted in both the transverse and longitudinal directions of the reinforcement independently by coupling the axial forces of the membranes. The precast deck panels had two layers of reinforcement with No. 19 (No. 6) bars spaced at 153 mm (6.0 in.) on center in both directions. To create an equivalent smeared reinforcement layer the membrane elements were given a uniform thickness of 3.76 mm (0.148 in.)

The two layers of reinforcement required that three concrete volumes be created: one above, between, and below the reinforcement layers. Keypoints were defined and volumes were constructed. Two more volumes were created using the BLOCK

command for the bearings. All volumes were glued together with the VGLUE command. The purpose of this command is to ensure that the volume interfaces are meshed with consistent nodes.

The concrete slab volumes were then attributed with the concrete material and SOLID65 element type. The volume was meshed using the VSWEEP command. The areas shared between the three layers of concrete volumes were attributed with the steel material and SHELL181 element type. These areas were meshed with the AMESH command. The two steel bearing volumes were attributed with the steel material and SOLID65 element type. The volumes were meshed.

The nodes on the bottoms of the steel bearings were assigned zero displacements in all three directions. Also, it was determined that the grouted shear key along the adjacent transverse joints contributed to the vertical boundary conditions of the panel. The vertical displacement of the edges along the transverse was set to zero.

The transverse joint model was more complex than the continuous panel model. Two adjacent panels were created with the same characteristics as the continuous panel model. Strips of steel bearing elements supported both panels on opposing edges. The panels were connected together by a transverse joint. A grout material was defined with a compressive strength of 34.5 MPa (5,000 psi) and a tensile strength of 3,650 kPa (530 psi). The grout volume did not share nodes with the adjacent panels; instead, contact pairs were set up to connect the two using TARGE170 and CONTA173 element types. The bond between the grout and concrete was modeled with a cohesive zone material (CZM). This material was assigned to the contact elements. The CZM models nonlinear

contacts with a de-bonding mechanism. De-bonding can occur in the normal and tangential directions of the contact surfaces. Since the primary de-bonding failure was a normal separation of the grouted key from the concrete, the tangential separation criteria was neglected. Previous research (Julander, 2009) has implemented a maximum tensile stress of 758 kPa (110 psi) as the concrete/grout bond strength, and that value was used here. The final criterion describing de-bonding is the separation distance which was set to 0.25 mm (0.01 inches). This means that when the tensile stress of the bond interface reached the maximum allowed value, the contact separated that distance and no force was further transmitted across the connection.

The final aspect of the transverse joint model was the usage of LINK8 elements as the shear keys. The shear keys used in the 8th North Bridge replacement consisted of two 13 mm (0.5 in.) diameter steel rods. Accordingly, the link elements were given a cross sectional area of 95.5 mm^2 (0.148 in^2). Two links were used between the panels halfway between the girder supports and spaced a distance of 152 mm (6.0 in.) apart. The finalized mesh is shown in Figure 47.

The transverse joint model was supported in the same manner as the continuous panel model with the exception of the adjacent panel shear keys. In both models, a force was applied to the top of the deck over an area approximately consistent with that of the spherical bearing. The overall force was distributed among nodes according to tributary areas. For both models the nonlinear force convergence control was activated. A tolerance of 0.05% about a minimum reference value of 0.01 was used.

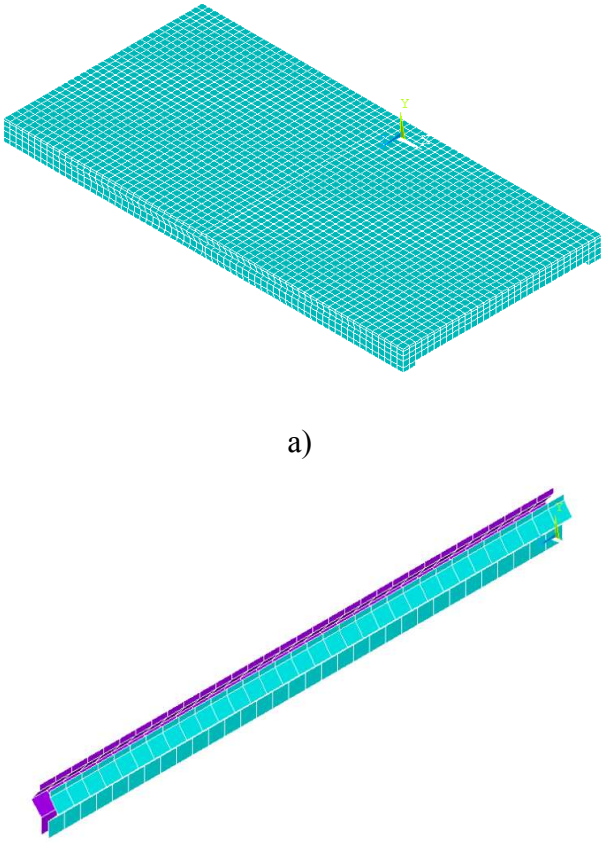

a)

b)

Figure 47. a) Transverse joint model mesh and b) contact elements at joint.

Results and comparison

Ultimate loads were applied to the continuous panel model at the center of the panel, halfway between the girder supports. The load was automatically divided into increments based on the program's nonlinear predictor. Results were written for each load step. Among the highest interest of all results was the cracking sequence.

The cracking of concrete in *ANSYS* is predicted at integration points of individual elements. When the principle tensile stress exceeds a user-defined limit, the element is considered cracked at that point. Mathematically, the cracked region of the element is

assigned a zero stiffness and the overall material properties are modified accordingly. Cracks may occur in three orthogonal directions. For post-processing convenience, *ANSYS* plots the sequence of cracks at an integration point by colors: red (first), green (second), and blue (third). The cracks are plotted as a circle oriented on the plane of the crack. If a crack opens and then closes, it is plotted as a circle with an 'X' through it.

Much of the cracking predicted by the software was isolated to the center of the panel beneath the applied load. Cracking initiated along the underside of the panel where the bending moment and hence greatest tensile stresses were highest. As the load increased shear cracks started to propagate in a conical fashion away from the applied load. The boundary conditions included some degree of fixity at the girder supports and therefore a small negative moment region was induced. At approximately 95% of the applied load the negative moment region produced tensile cracks along the top of the deck. Finally, at 657 kN (148 ^{k}) a complete failure surface was encountered through the depth of the deck and failure was reached (Figure 48 and Figure 49).

a) b)

Figure 48. Punching shear failure comparison: a) experimental panel and b) FEM panel.

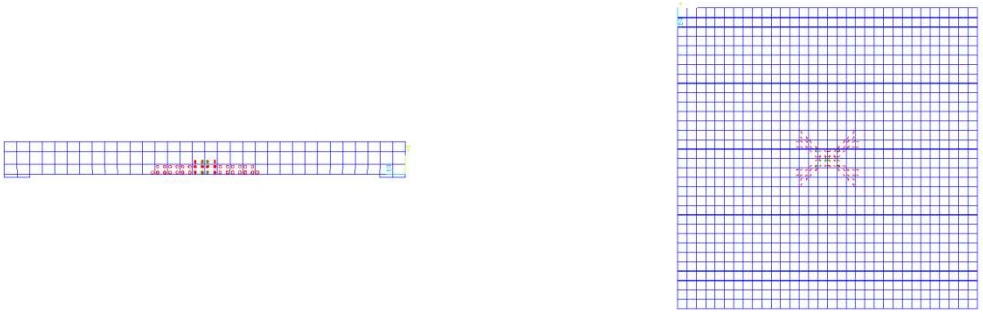

a) 203 kN (45.6^{k})

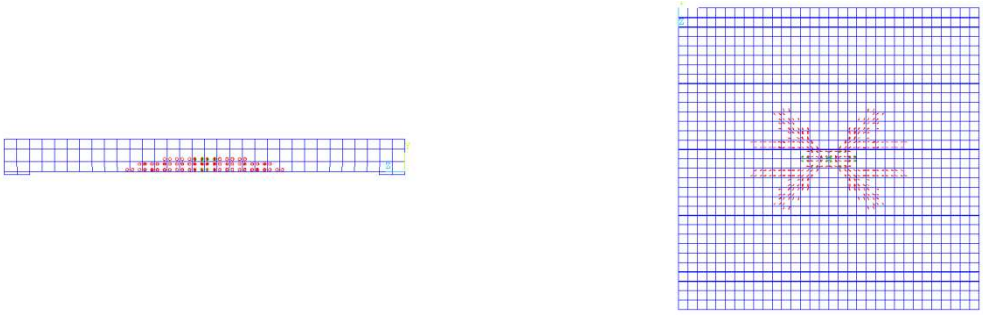

b) 326 kN (73.3^{k})

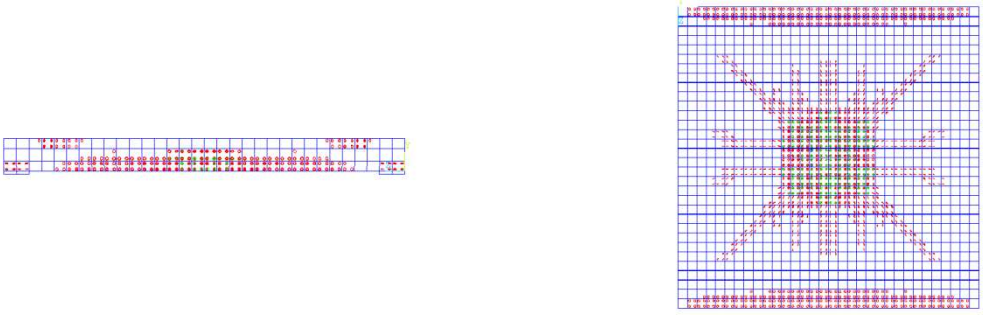

c) 635 kN (143^{k})

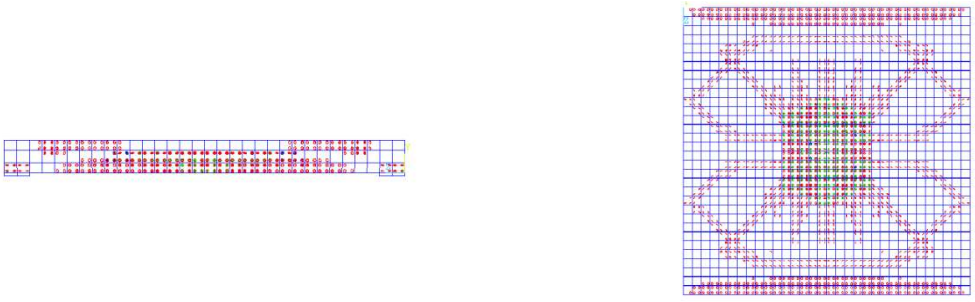

d) 657 kN (148^{k})

Figure 49. Cracking sequence of continuous panel model (profile on left, plan on right).

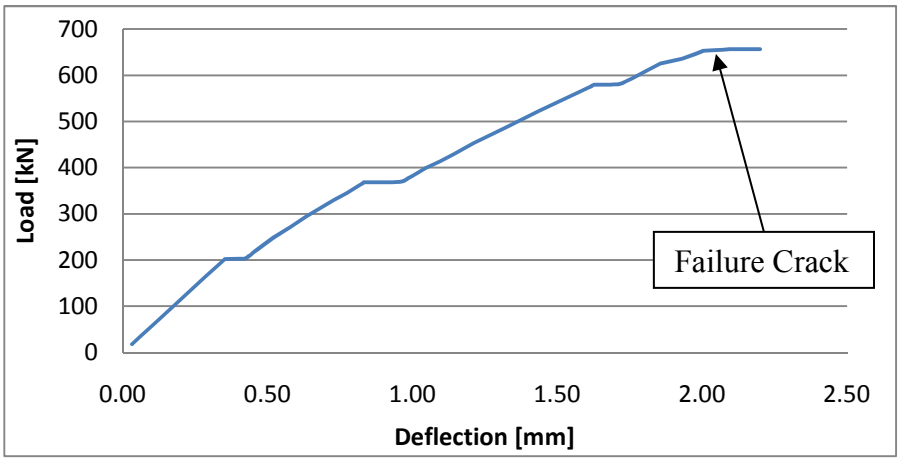

Figure 50. Load-deflection plot for panel punching shear.

Failure of the deck can be verified by examining a load-deflection plot. Figure 50 shows such a plot for a node that lies directly beneath the applied load. It can be seen that at a certain point the deflection increases with a zero slope (i.e. zero stiffness). This point coincides with the assumed ultimate load. The ultimate load predicted by the continuous panel FEM was 8.3% lower than the average measured ultimate load.

The transverse joint model behaved considerably different than the continuous panel model. There was much less concrete cracking throughout the failure sequence (Figure 51). A much smaller failure surface throughout the depth of the deck was reached at a much smaller load, 372 kN (83.6^{k}), which is 4.1% smaller than the average measured ultimate load. The failure surface was more cylindrical than conical. There was also much de-bonding of the contact and target elements connecting the grouted key to the concrete. The de-bonding was predicted towards the bottom portion of the joint. This can be seen by plotting the deformed shape of the FEM (Figure 52).

a) 194 kN (43.6^{k})

b) 283 kN (63.6^{k})

c) 372 kN (83.6^{k})

Figure 51. Cracking Sequence of transverse joint panel model.

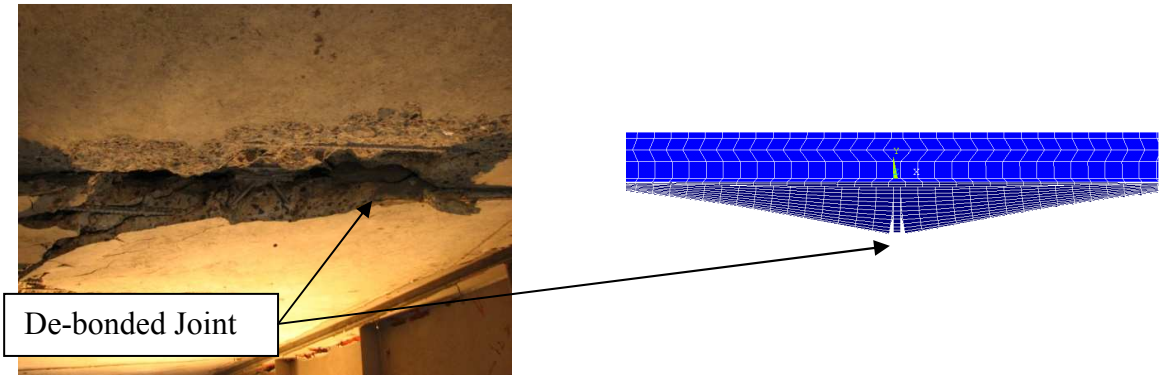

a) b)

Figure 52. De-bonding of transverse joint comparison: a) experimental and b) FEM.

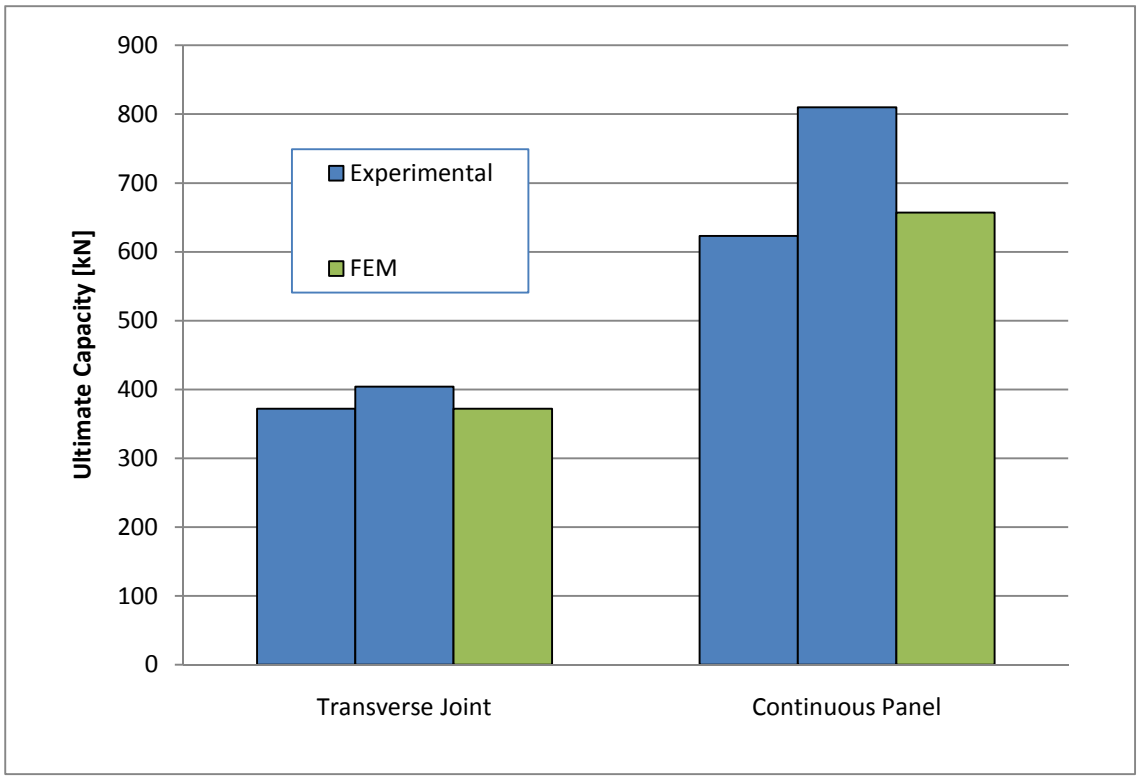

Figure 53. Punching shear capacity comparison.

Both the continuous panel and transverse joint FEMs produced results consistent with that of experimental findings (Figure 53). Results from finite element analysis on the transverse joint model yielded an ultimate punching shear capacity that was 43% lower than the continuous panel model. This compared very well to the 46% difference in ultimate punching shear capacities witnessed in the laboratory.

CHAPTER V

CONCLUSIONS

Full-scale bridge destructive testing is incredibly rare. Aside from requiring funding and proper laboratory settings, the supply of in-tact, full-scale specimens is extraordinary. Accordingly, the results from said testing are invaluable. Two full-scale bridge specimens consisting of steel girders and precast deck panels were subjected to three failure tests. The investigated failure modes were flexural, beam shear, and punching shear. The bridge failures were replicated using *ANSYS* software.

A flexural failure was obtained in the laboratory by applying a point load to the bridge specimen with a hydraulic ram. Recorded changes in strains on the girders indicated that the elastic N.A. did not coincide with the theoretical N.A., which suggested that the girders and deck were not acting completely composite. The primary failure mechanism was concrete splitting due to insufficient development length of longitudinal reinforcement. Subsequent analysis yielded an approximate compressive stress in the concrete at the initiation of the splitting failure. A FEM was constructed using solid elements for the deck and shell elements for the girders. The deck was modeled as a monolithic feature rather than individual panels. An elastic- plastic material model was implemented for concrete with a yield stress equal to the approximate concrete compressive stress upon initiation of the splitting failure. The girders were connected to the deck by contact elements that transferred 50% of the shear flow between them. The deflection comparison between the experimental and analytical models showed great correlation. The FEM predicted an ultimate load which was lower than the experimental

ultimate load by 3.4%. In the experimental and analytical model, the unloaded girder carried a maximum of -1.6% and -3.2 % of the applied load (uplift), respectively. The average of the calculated maximum moments for the two experimental tests was lower than the FEM approximated moment by 0.2%.

A beam shear failure was obtained in the laboratory by applying a point load with a hydraulic ram near a reaction. Strain gages mounted on the girder web recorded the first yield at a load level that was extremely close to the ultimate sustained load. At this load level, the web began to buckle. A post-tension buckling strut formed and grew in out-of-plane deflection for the remainder of the test. A FEM was conducted using the same modeling criteria as the flexural model (solid elements for the concrete deck and shell elements for the girders). The only difference between the models was a mesh refinement in the area near the applied load. To predict the failure mode witnessed in the laboratory, it was necessary to conduct a nonlinear buckling analysis. For this type of analysis, the program incrementally applied load until the model became unstable, which was determined to be a buckling failure. The buckling load predicted by the FEM was 5.3% greater than measured in the experimental model. Furthermore, the ultimate reaction force nearest the applied load (i.e. the approximate shear force on the cross section) predicted by the FEM was 4.6% greater than the experimentally measured shear force at buckling failure. Also, the load-deflection curves for both the experimental and analytical models show good agreement up to the buckling failure.

The last failure mode investigated in the laboratory was punching shear of the deck panels. In all, four punching shear tests were conducted. For two of the tests, point

loads were applied near the middle of a deck panel and approximately mid-way between the girders. For the other two tests, point loads were applied directly above a transverse joint between two panels and approximately mid-way between the girders. The two types of tests produced different failures. For the continuous panel test, the predicted failure surface was conical in shape and radiated outward from the applied load. For the transverse joint model, the failure surface was very isolated near the applied load. There was less concrete cracking compared to the continuous panel model. There was also de-bonding of the grout/concrete interface along the transverse joint. There was an average 46% difference in the measured ultimate punching shear capacities between the two types of tests, with the transverse joint tests yielding the lower capacities. Two FEMs were created and analyzed: one with loading at the center of the deck panel and one with loading at the transverse joint of the panel. The models consisted of solid elements with a brittle concrete material model, which predicts cracking and crack propagation. Reinforcement was modeled as smeared membrane elements layered within the solid elements. The concrete-grout bond was modeled with a cohesive zone material which fails upon a user-specified tensile stress. The shear key was modeled with simple link elements. The continuous panel FEM predicted an ultimate shear capacity which was 8.3% lower than the average measured shear capacity. The transverse joint FEM predicted an ultimate shear capacity which was 4.1% lower than the average measured shear capacity. The punching shear FEMs predicted a 43% difference in punching shear capacities, with the transverse joint model yielding the lower capacity. Also, the failures predicted in the FEMs closely resemble those observed in the laboratory. For the

continuous panel model, a conical failure surface was formed through the depth of the deck surrounding the applied load. For the transverse joint model, there was comparatively less cracking, and the cracking was more isolated near the applied load. The FEM also predicted de-bonding of the grout/concrete along the transverse joint. All of these predicted failures agree with experimental observations.

The final objective of this research was to examine changes in dynamic behavior throughout flexural yield and failure. This was done by incrementally applying point loads and conducting modal analysis between each load increment. Velocity transducers were mounted to the bridge deck and a forced excitation was provided by a vertical shaking device. The signals were processed and the frequency response spectrum was analyzed. Three natural frequencies and corresponding mode shapes were monitored for each dynamic test. It was found that progressive yield of the girders corresponded to a slight increase in natural frequencies. The first recorded yield of the system resulted in an average increase in the three monitored natural frequencies of 1.3%. The next two load increments also resulted in increases in natural frequencies, although to a lesser extent. In other words, the system became stiffer as the degree of flexural yield was increased. At one load increment, a horizontal crack developed in the concrete deck which followed the top layer of reinforcement. This produced a decrease in average natural frequencies of 1.0%. Deck damage was increased during the next two load increments which resulted in decreases in average natural frequencies of 1.3 and 5.8%, respectively. Fifteen dynamic tests were conducted total, and there was an overall decrease in average natural frequencies of 5.4%. It is also expected that temperature

effects were a factor among all natural frequencies recorded as the testing was performed over a two day time period.

REFERENCES

ACI Committee 318. 2008. Building code requirements for structural concrete (ACI318-08) and commentary. American Concrete Institute, Farmington Hills, Michigan.

ANSYS, Inc. 2005a. ANSYS commands reference. S.A.S. IP Inc., Canonsburg, Pennsylvania.

ANSYS, Inc. 2005b. ANSYS elements reference. S.A.S. IP Inc., Canonsburg, Pennsylvania.

Askegaard, V., and P. Mossing. 1988. Long term observation of RC-bridge using changes in natural frequencies. Selected papers, Nordic Concrete Research, Publication No. 7: 20-27.

Barbosa, A. F., and G. O. Ribeiro. 1998. Analysis of reinforced concrete structures using ANSYS nonlinear concrete models. Federal University of Minas Gerais, Barcelona, Spain. 7 p.

Chen, H. L., C. C. Spyrakos and G. Venkatesh. 1995. Evaluating atructural deterioration by dynamic response. Journal of Structural Engineering 121(8): 1197-1204.

Cook, W. J. 2010. Destructive testing of composite precast concrete deck panels and built-up steel plate girders. Unpublished MS Thesis. Utah State University Library, Logan, Utah. 110 p.

Data Physics Corporation. 2006. SignalCalc dynamic signal analyzer user manual. Data Physics Corporation, San Jose, California.

Fu, K. C. and F. Lu. 2003. Nonlinear finite-element analysis for highway bridge superstructures. Journal of Bridge Engineering 8(3): 173-179.

Issa, M. A., R. Anderson, T. Domagalski, S. Asfour, and M.S. Islam. 2007. Full-scale testing of prefabricated full-depth precast concrete bridge deck panel system. ACI Structural Journal 104(3): 324-332.

Julander, J. L. 2009. Finite-element modeling of full depth precast concrete transverse bridge deck connections. MS Thesis. Utah State University Library, Logan, Utah. 86 p.

Lauzon, R. G., and J. T. DeWolf. 2006. Ambient vibration monitoring of a highway bridge undergoing a destructive test. Journal of Bridge Engineering 11(5): 602-310.

Mabsout, M. E., K. M. Tarhini, G. R. Frederick, and C. Tayar. 1997. Finite-element analysis of steel girder highway bridges. Journal of Bridge Engineering 2(3): 83-87.

Utah Department of Transportation (UDOT). 2006. 800 north over I-15 precast deck replacement Plans. UDOT Structures Division, Salt Lake City, Utah. 26 p.

Zhao, J. and J. T. DeWolf. 2002. Dynamic monitoring of steel girder highway bridge. Journal of Bridge Engineering 7(6): 350-356.